CHAPTER 5

CONSIDERATION OF THE MAGNETIC SATURATION EFFECT ON THE PROPOSED LTC

5.1 Introduction

The theoretical basis of the linear maximum torque per ampere control strategy for an IPMSM drive has been presented in the previous chapter. Because the rotor permanent magnets are embedded inside the rotor core and the direction of the d-axis is oriented toward the field direction of the N-pole of the rotor permanent magnet, the resulting d-axis effective air-gap length is larger than the resulting q-axis effective air-gap length. Hence, the q-axis flux linkage tends to saturate under the operation conditions of large q-axis current. However, due to the larger reluctance, the corresponding d-axis flux linkage still shows a relatively linear magnetic characteristic with respect to the d-axis current [14, 31, 33, 50, 55]. Thus, further investigation about the saturation effect on the dynamic as well as the steady state performances for a high performance vector controlled IPMSM drive system becomes the major motivation of this chapter.

In this chapter, a more accurate model for the q-axis flux linkage is proposed to cover saturation effect and the corresponding LMTPA control strategy is derived. Then the effects of the magnetic saturation on the dynamic and the steady state performances for the tested IPMSM drive system are examined via some experimental tests. For comparison of the performances of the proposed saturated model with that of the linear magnetic model, the same prototype as constructed in the previous chapter is used to conduct the experimental tests. Concerning implementation, the previously developed control programs in the DSP are

modified to implement the proposed control, then some experimental results are provided to show the merits of the proposed control strategy.

5.2 Saturated Model of An IPMSM

For convenience, the dynamic model [66] of an IPMSM in the rotor reference frame will be repeated as follows:

$$v_{ds} = \mathrm{R_S}\, i_{ds} + \frac{d\lambda_{ds}}{dt} - \omega_r \lambda_{qs} \tag{5.1}$$

$$v_{qs} = \mathrm{R_S}\, i_{qs} + \frac{d\lambda_{qs}}{dt} + \omega_r \lambda_{ds} \tag{5.2}$$

$$\lambda_{ds} = \lambda_d + \lambda_{\mathrm{mf}} \tag{5.3}$$

$$T_{\mathrm{e}} = \frac{3}{2}\frac{\mathrm{p}}{2}\left[\, \lambda_{ds}\, i_{qs} - \lambda_{qs}\, i_{ds} \,\right] \tag{5.4}$$

where

v_{ds}, v_{qs} : stator d- and q-axis voltages respectively

i_{ds}, i_{qs} : stator d- and q-axis currents respectively

$\mathrm{R_S}$: stator winding resistance

λ_{ds}, λ_{qs} : stator d- and q-axis flux linkages respectively

λ_{mf} : d-axis flux linkage resulting from the rotor permanent magnet

λ_d : d-axis flux linkage resulting from the i_{ds}

ω_r : electrical angular frequency

T_e : electromagnetic torque

p : number of poles

As can be seen from Chapter 2, under linear magnetic condition, the above λ_{ds}, λ_{qs}, and T_e should become (2.3), (2.4), and (2.5) respectively. However, the q-axis saturated effect of the IPMSM should be considered to further elevate the performances of the drive system. Under steady state, λ_{ds} and λ_{qs} become constants and (5.1) and (5.2) reduce to the following forms:

$$v_{ds} = \mathrm{R_S}\, i_{ds} - \omega_r\, \lambda_{qs} \tag{5.5}$$

$$v_{qs} = \mathrm{R_S}\, i_{qs} + \omega_r\, \lambda_{ds} \tag{5.6}$$

Since for an IPMSM, the effective air-gap length of the d-axis is relatively larger than that of the q-axis, the magnetic saturation can be assumed to be negligible. The corresponding d-axis inductance $\mathrm{L_d}$ is then assumed to be constant. On the contrary, the effective air-gap length of the q-axis is relatively smaller than that of the d-axis, the corresponding magnetic saturation is more significant for a variable speed IPMSM drive system [14, 31, 33, 50, 55]. Therefore, the d- and q-axis flux linkages respectively are chosen to be:

$$\lambda_{ds} = \lambda_d + \lambda_{\mathrm{mf}} \triangleq \mathrm{L_d}\, i_{ds} + \lambda_{\mathrm{mf}} \tag{5.7}$$

$$\lambda_{qs}(i_{qs}) \triangleq a\, i_{qs}^3 + b\, i_{qs}^2 + c\, i_{qs} \tag{5.8}$$

where λ_d is assumed to be proportional to i_{ds}, the factor $\mathrm{L_d}$ is the linear d-axis inductance as defined in Chapter 2, and the λ_{qs} is expressed as a third order polynomial function of the q-axis current i_{qs}. The corresponding coefficients of a, b, and c in (5.8) are real constants respectively. For reference, Fig. 5.1 shows the measured λ_{qs} vs. i_{qs} plot for the tested IPMSM that is a prototype designed in [67]. As can be seen from Fig. 5.1, the asterisks denote the measured points of λ_{qs} and the solid line is the corresponding fitted curve of λ_{qs}.

Table 5.1 also lists the numerical values of a, b, and c in (5.8) respectively as well as the other motor parameters and the inverter ratings.

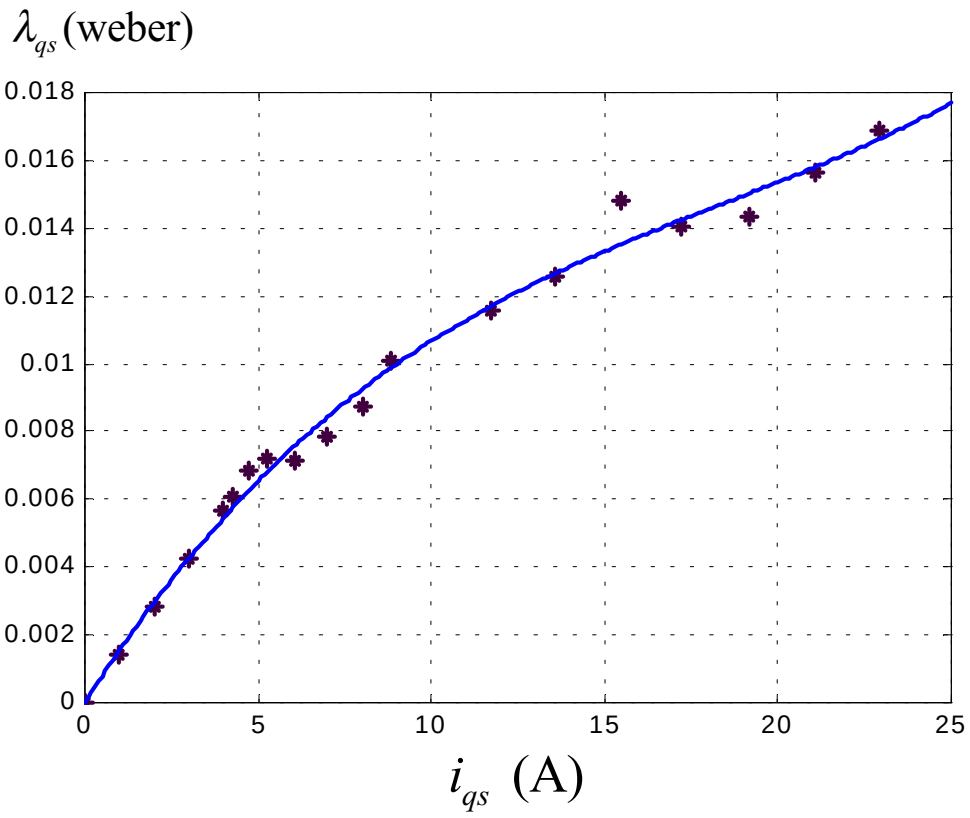

Fig. 5.1. The measured λ_{qs} to i_{qs} points and the corresponding fitted curve of λ_{qs}.

Table 5.1. The Tested IPMSM Parameters and Inverter Ratings.

parameters \ tested IPMSM	
number of poles	6
armature resistance (Ω)	0.15
d-axis inductance (mH)	0.488
magnetic flux linkage (V/(rad/sec))	0.042
maximum phase voltage amplitude V_{SM} (V)	50
maximum phase current amplitude I_{SM} (A)	25.0
coefficient of "a" in (5.8)	1.1939×10^{-6}
coefficient of "b" in (5.8)	-6.5801×10^{-5}
coefficient of "c" in (5.8)	1.6065×10^{-3}

5.3 The Proposed Linear Maximum Torque Per Ampere Control Considering Magnetic Saturation

As the saturated model of an IPMSM is concerned, the LMTPA control strategy proposed in the previous chapter should be modified.

5.3.1 Constant Torque Limit Region

By substituting (5.7) and (5.8) into (5.4), one can obtain

$$T_e = \frac{3}{2}\frac{p}{2}\left[(L_d i_{ds} + \lambda_{mf}) i_{qs} - (a i_{qs}^3 + b i_{qs}^2 + c i_{qs}) i_{ds} \right] \tag{5.9}$$

Following from (5.9), the d-axis current becomes

$$i_{ds} = \frac{T_e/(0.75\mathrm{p}) - \lambda_{\mathrm{mf}}\, i_{qs}}{(\mathrm{L_d} - a\, i_{qs}^2 - b\, i_{qs} - c)\, i_{qs}} \tag{5.10}$$

Define

$$h(i_{qs}) \triangleq i_{ds}^2 + i_{qs}^2 = \frac{[T_e/(0.75\mathrm{p}) - \lambda_{\mathrm{mf}}\, i_{qs}]^2}{[(\mathrm{L_d} - a\, i_{qs}^2 - b\, i_{qs} - c)\, i_{qs}]^2} + i_{qs}^2 \tag{5.11}$$

For a given torque T_e, in order to derive the maximum torque per ampere control, one can take the derivative of (5.11) as follow:

$$\frac{dh(i_{qs})}{di_{qs}} = \frac{\{(a\, i_{qs}^2 + b\, i_{qs} + c - \mathrm{L_d})\, i_{qs}\, \lambda_{\mathrm{mf}} - [T_e/(0.75\mathrm{p}) - \lambda_{\mathrm{mf}}\, i_{qs}](\mathrm{L_d} - 3ai_{qs}^2 - 2bi_{qs} - c)\}}{0.5[(\mathrm{L_d} - a\, i_{qs}^2 - b\, i_{qs} - c)\, i_{qs}]^3}$$

$$[T_e/(0.75\mathrm{p}) - \lambda_{\mathrm{mf}}\, i_{qs}] + 2i_{qs} \tag{5.12}$$

Then substituting (5.9) into (5.12), the resulting reduced formula becomes

$$\frac{dh(i_{qs})}{di_{qs}} = \frac{(\mathrm{L_d} - 3ai_{qs}^2 - 2bi_{qs} - c)i_{ds}^2 + \lambda_{\mathrm{mf}}\, i_{ds} + (a\, i_{qs}^2 + b\, i_{qs} + c - \mathrm{L_d})\, i_{qs}^2}{0.5(a\, i_{qs}^2 + b\, i_{qs} + c - \mathrm{L_d})\, i_{qs}} \tag{5.13}$$

By letting the numerator of (5.13) be equal to zero, one can obtain the following equation:

$$(\mathrm{L_d} - 3\, a\, i_{qs}^2 - 2\, b\, i_{qs} - c)\, i_{ds}^2 + \lambda_{\mathrm{mf}}\, i_{ds} + (a\, i_{qs}^2 + b\, i_{qs} + c - \mathrm{L_d})\, i_{qs}^2 = 0 \tag{5.14}$$

The solution of (5.14) is the $i_{ds} \sim i_{qs}$ relation to achieve maximum torque per ampere (MTPA) control and is derived as

$$f(i_{ds}, i_{qs}) = 2(3a i_{qs}^2 + 2b i_{qs} + c - L_d) i_{ds} - \lambda_{mf} + \sqrt{\lambda_{mf}^2 - 4 i_{qs}^2 (3a i_{qs}^2 + 2b i_{qs} + c - L_d)(L_d - a i_{qs}^2 - b i_{qs} - c)} = 0 \quad (5.15)$$

Under linear magnetic condition, the coefficients a, b, and c of (5.8) become 0, 0, and L_q respectively where L_q is the linear q-axis inductance as defined in Chapter 2. Then the resulting λ_{qs} is equal to (2.4) and one can also check that (5.15) reduces into (4.1). Furthermore, in order to guarantee the value of i_{ds} in (5.15) is negative for $i_{qs} \geq 0$, the following condition should be satisfied:

$$a i_{qs}^2 + b i_{qs} + c > L_d \quad (5.16)$$

As the tested IPMSM drive is concerned, the range of $(a i_{qs}^2 + b i_{qs} + c) \in (0.75, 1.6)$ mH and L_d=0.488 mH over the full operational ranges of d- and q-axis currents. Thus the condition of (5.16) is indeed satisfied for the tested IPMSM drive system. When the maximum line current magnitude I_{sm} is imposed, namely

$$i_{ds}^2 + i_{qs}^2 = I_{sm}^2 \quad (5.17)$$

Then the intersection point of (5.15) and (5.17) denoted as (I_{dsM}, I_{qsM}) can be obtained. Therefore, the maximum available torque, T_{eM} within the current limit is expressed as:

$$T_{eM} = 0.75\,p\,[(L_d I_{dsM} + \lambda_{mf}) I_{qsM} - (a I_{qsM}^3 + b I_{qsM}^2 + c I_{qsM}) I_{dsM}] \quad (5.18)$$

Also, the corresponding angular speed ω_{rM} can be calculated from the following equation by substituting (5.5) ~ (5.8) as well as I_{dsM} and I_{qsM} into the voltage boundary equation:

$$[\mathrm{R_s} I_{dsM} - \omega_{rM}(aI_{qsM}^3 + b\, I_{qsM}^2 + cI_{qsM})]^2 + \left[\mathrm{R_s} I_{qsM} + \omega_{rM}(\mathrm{L_d} I_{dsM} + \lambda_{\mathrm{mf}})\right]^2 = \mathrm{V_{sm}^2} \quad (5.19)$$

Next, in order to achieve a linear control law, a virtual control u^* corresponding to a torque command T_e^* can be defined as follows:

$$u^* \triangleq \frac{T_e^*}{\mathrm{K_{tM}}} = \frac{0.75\ \mathrm{p}\ [(\mathrm{L_d} i_{ds}^* + \lambda_{\mathrm{mf}}) i_{qs}^* - (a i_{qs}^{*\,3} + b\, i_{qs}^{*\,2} + c i_{qs}^*) i_{ds}^*]}{\mathrm{K_{tM}}} \quad (5.20)$$

where the torque constant $\mathrm{K_{tM}}$ is chosen to be

$$\mathrm{K_{tM}} \triangleq \frac{T_{eM}}{\mathrm{I_{sm}}} \quad (5.21)$$

As will be clear from later sections, the same torque constant $\mathrm{K_{tM}}$ is used not only in the constant torque limit range but also in the entire field weakening range. For convenient explanation of the proposed linear maximum torque per ampere (LMTPA) control considering magnetic saturation, define Region I as the constant torque limit region where $\omega_r < \omega_{rM}$. Hence, in this region, if a torque command $T_e^*(=\mathrm{K_{tM}}\, u^*)$ is given, then the corresponding d- and q-axis current commands can be solved from the simultaneous equations of (5.15) and (5.20). The corresponding solutions of i_{ds}^* and i_{qs}^* can not be expressed by closed forms, however they can be obtained easily by using any available commercial numerical program with proper initial values. For reference, the trajectories of $i_{ds}^* \sim u^*$ and $i_{qs}^* \sim u^*$ adopted in the constant torque limit region for the tested IPMSM are shown in Fig. 5.2.

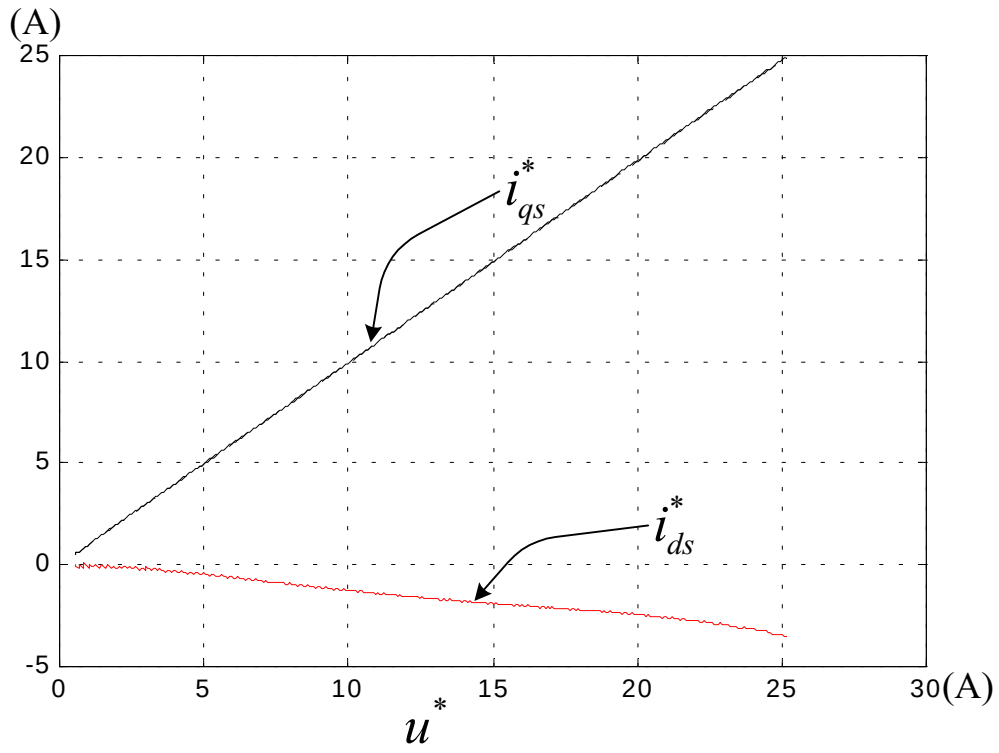

Fig. 5.2. The trajectories of $i_{ds}^* \sim u^*$ and $i_{qs}^* \sim u^*$ adopted in the constant torque limit region for the tested IPMSM.

For clarity, the trajectory of (5.15) on the $i_{ds}^* \sim i_{qs}^*$ plane, namely AIO curve, is shown in Fig. 5.3 where the current limit curve and one constant torque curve together with five voltage limit curves for the tested IPMSM are also shown on the same figure. In summary, in Region I, given a torque command T_e^*, one can get the corresponding virtual control u^* from (5.20). Then, from u^* one can obtain the corresponding i_{ds}^* and i_{qs}^* from Fig. 5.2. Although the generated torque command T_e^* as in (5.9) is still nonlinear to i_{ds}^* and i_{qs}^*, but it is now proportional to the virtual control u^* as in (5.20). Thus, excluding the inner current loop control, the outer loop controller can be easily designed by using any existing linear control strategy directly.

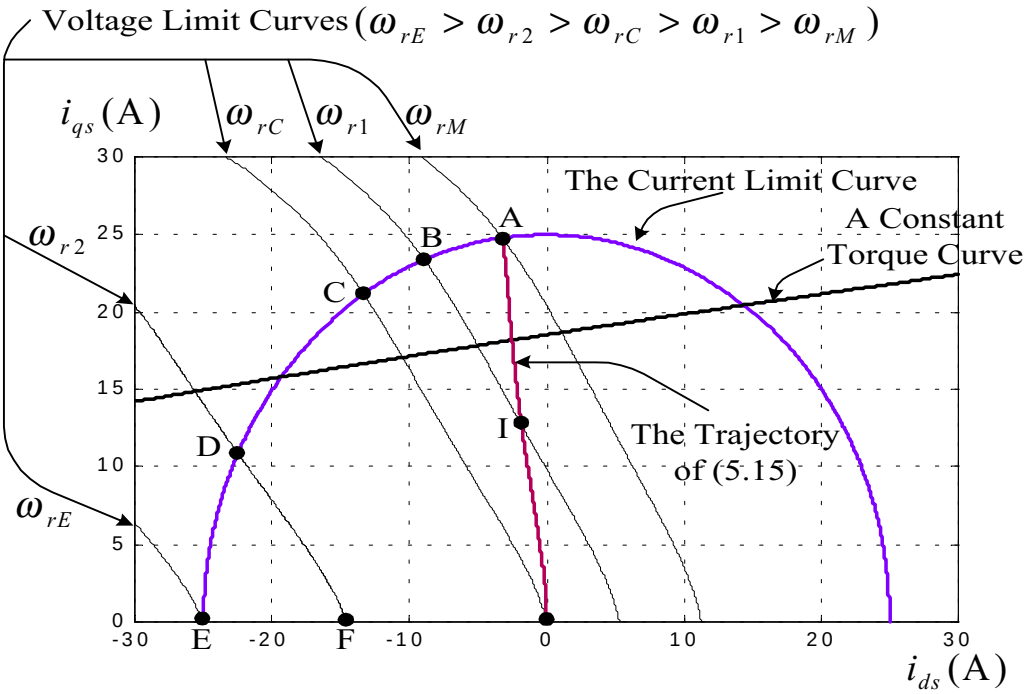

Fig. 5.3. The trajectories of (5.15), the current limit curve, one constant torque curve, and five voltage limit curves on i_{ds}-i_{qs} plane for the tested IPMSM.

5.3.2 Partial Field Weakening Region and Full Field Weakening Region

From the previous section, it is seen that during acceleration, for $\omega_r < \omega_{rM}$, one can select the maximum torque T_{eM} to achieve the fastest response. However, when $\omega_r > \omega_{rM}$, due to the current and voltage constraints of (2.21) and (2.22), the maximum torque (T_{eM}) can not be achieved. The traditional control strategy is simply to reduce the magnetic field intensity by applying negative d-axis stator current resulting in the so called field weakening control. As can be observed from Fig. 5.3, as far as the current constraint is concerned, the field weakening region is bounded by the ABCDE curve, the AIO curve, and the EO axis. In particular, four points (namely B, C, D, and E) are also marked in Fig. 5.3, where the voltage limit curves are also imposed on, namely

$$v_{ds}^2 + v_{qs}^2 = \mathrm{V}_{\mathrm{sm}}^2 \tag{5.22}$$

By substituting (5.5) ~ (5.8) into (5.22), one can obtain:

$$g(i_{ds}, i_{qs}, \omega_r) \triangleq [\mathrm{R_S}\, i_{ds} - \omega_r (a\, i_{qs}^3 + b\, i_{qs}^2 + c\, i_{qs})]^2 + [\mathrm{R_S}\, i_{qs} + \omega_r (\mathrm{L_d}\, i_{ds} + \lambda_{\mathrm{mf}})]^2 - \mathrm{V_{sm}^2} = 0 \tag{5.23}$$

Thus, from (5.23), it is seen that when $i_{ds} = i_{qs} = 0$, then one can obtain the corresponding speed, called the critical angular frequency ω_{rC} that is the same as (3.3) for the same IPMSM and the drive specifications. Similarly, also from (5.23), when $i_{ds} = -\mathrm{I_{sm}}$ and $i_{qs} = 0$ then one can obtain the corresponding speed, called the extreme angular frequency ω_{rE} that is also the same as (3.4) for the same IPMSM and the drive specifications.

The corresponding boundary operating points of ω_{rC} and ω_{rE} on the $i_{ds} \sim i_{qs}$ plane are just the C and E points marked in Fig. 5.3. Also, from (3.4), one can see that to get positive value of ω_{rE}, it is necessary that λ_{mf} be greater than $\mathrm{L_d I_{sm}}$. Indeed, for the tested IPMSM, $\mathrm{L_d}\,|i_{ds}|$ is always less than λ_{mf} within the operable range. Further examination of Fig. 5.3 reveals that when the motor speed $\omega_r \in (\omega_{rM}, \omega_{rC})$, then the voltage bound curve of (5.23) will intersect with the AIO curve. For example, Fig. 5.3 shows a voltage bound curve for $\omega_r = \omega_{r1}$, and the corresponding intersecting point is I. In other words, for each given $\omega_r \in (\omega_{rM}, \omega_{rC})$, the corresponding boundary currents i_{dsb} and i_{qsb} of point I can be solved from system of equations of (5.15) and (5.23) as

$$f(i_{dsb}, i_{qsb}) = 0 \tag{5.24}$$

$$g(i_{dsb}, i_{qsb}, \omega_r) = 0 \tag{5.25}$$

Hence, the corresponding electromagnetic torque bound and virtual control bound, namely

T_{eb} and u_b, can be defined as follows

$$T_{eb} \triangleq 0.75\,\mathrm{p}\,[(\mathrm{L_d} i_{dsb} + \lambda_{\mathrm{mf}}) i_{qsb} - (a\, i_{qsb}^3 + b\, i_{qsb}^2 + c\, i_{qsb}) i_{dsb}] \tag{5.26}$$

$$u_b \triangleq \frac{T_{eb}}{\mathrm{K_{tM}}} \tag{5.27}$$

Now it can be seen from Fig. 5.3 that when $\omega_r = \omega_{r1}$ and $T_e^* \le T_{eb}$, then despite that ω_{r1} is located in the conventional field weakening region, one can still use the maximum torque per ampere control, namely corresponding to the curve IO portion of Fig. 5.3, to achieve the minimum copper loss. Also the corresponding u^* as well as i_{ds}^* and i_{qs}^* remains the same as that obtained from Fig. 5.2. However, when $T_e^* > T_{eb}$, the intersecting point corresponding to the curve AI portion of Fig. 5.3 which is outside the voltage constraint, it is not possible to achieve the conventional maximum torque per ampere control. Therefore, the proposed control strategy chooses i_{ds}^* and i_{qs}^*, for a given T_e^* (and $u^* = \frac{T_e^*}{\mathrm{K_{tM}}}$) as the intersection point of the torque command equation (5.9) and the voltage boundary equation (5.23). Similar to the previous constant torque limit control, the corresponding d- and q-axis commands can be solved from the simultaneous equations of (5.20) and (5.23). Also, the solutions of i_{ds}^* and i_{qs}^* can not be expressed by closed forms. But they can be obtained easily by any available commercial program. In summary, for $\omega_r \in (\omega_{rM}, \omega_{rC})$, if $u^* < u_b$ (or equivalently $T_e^* < T_{eb}$), then the previous maximum torque per ampere control which is obtained from Fig. 5.2 can be applied. If $u^* > u_b$, then the field weakening control which is obtained from the solutions of (5.20) and (5.23) is applied. Since there are two control modes applicable in this speed range, it is called the partial field weakening region (Region II). It is worth mentioning that

within the partial field weakening region, the virtual control bound u_b is not a constant. It is varied with motor speed ω_r. For reference, Fig. 5.4 shows the trajectory of a virtual control bound within the partial field weakening region for the tested IPMSM as an illustration. Furthermore, for $\omega_r \in (\omega_{rC}, \omega_{rE})$, it is seen from Fig. 5.3 that it is not possible to have an intersection point for (5.15) and (5.23). Thus, for each torque command T_e^* (or equivalently u^*), the same field weakening control equations (5.20) and (5.23) are directly solved to find the corresponding i_{ds}^* and i_{qs}^*. Therefore, in this speed region, it is called the full field weakening region (Region III). For reference, Fig. 5.5 shows a schematic diagram for the maximum available torque with respect to the whole speed range for the tested IPMSM.

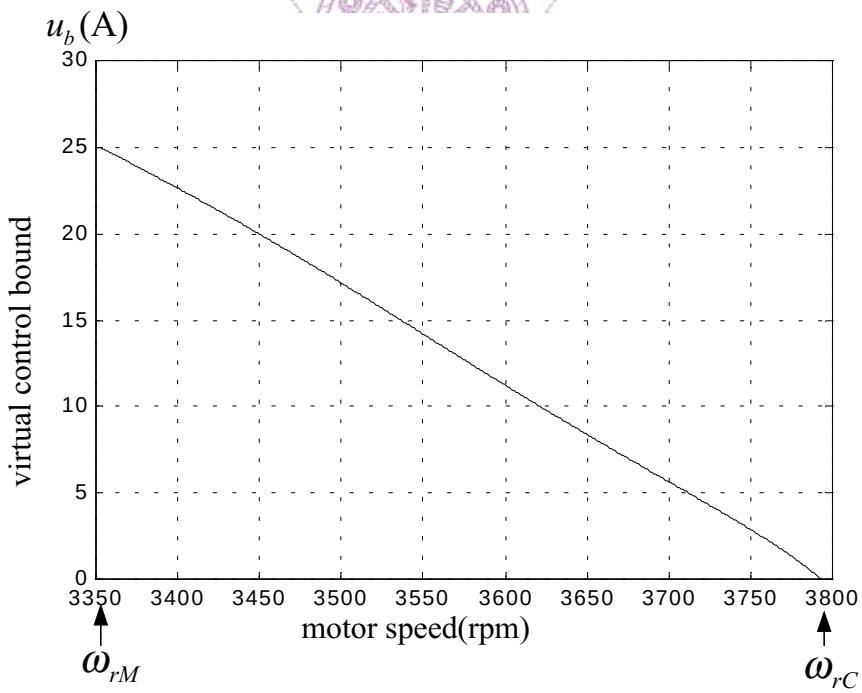

Fig. 5.4. Graphical illustration of the virtual control bound to motor speed curve for the tested IPMSM.

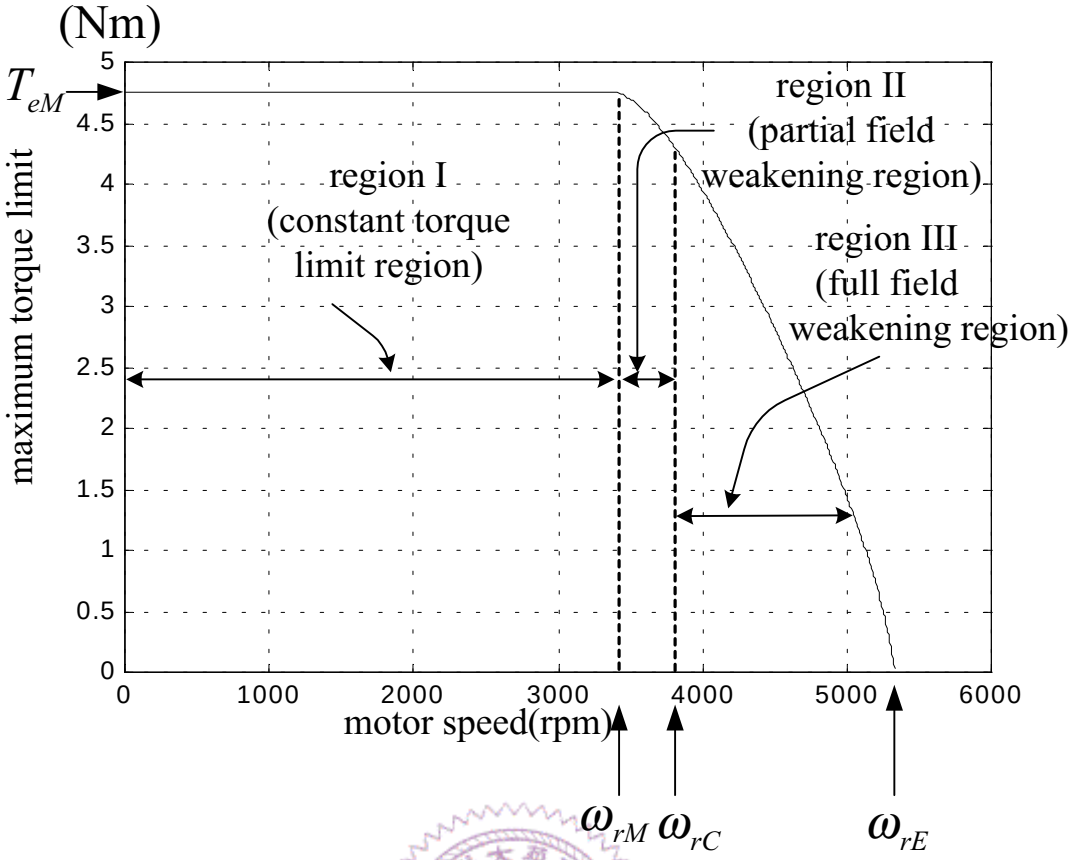

Fig. 5.5. Illustration of the maximum torque limit to motor speed curve and three operation regions for the tested IPMSM.

In fact, one of the characteristics of the proposed control strategy is that under transient condition, no matter in which region the operation speed is located, the maximum torque capability can always be applied to achieve the fastest response. From previous discussions, the proposed control strategy has been shown to be a linear one over the entire speed region. Also, for Region I and portion of Region II, the proposed control is identical with the maximum torque per ampere control to achieve minimum copper loss. It remains to prove that the proposed field weakening control can also achieve the minimum copper loss. From (5.15) one can see that the $i_{ds}^{*} \sim i_{qs}^{*}$ relation for the proposed maximum torque per ampere control can be rewritten as

$$i_{ds} = \frac{\lambda_{\mathrm{mf}} - \sqrt{\lambda_{\mathrm{mf}}^2 - 4(3ai_{qs}^2 + 2bi_{qs} + c - \mathrm{L_d})[(\mathrm{L_d} - c)i_{qs}^2 - bi_{qs}^3 - ai_{qs}^4]}}{2(3ai_{qs}^2 + 2bi_{qs} + c - \mathrm{L_d})} \tag{5.28}$$

Thus, when the proposed field weakening control is applied in either Region III or Region II for $T_e^* > T_{eb}$, it can be observed from Fig. 5.3 that the corresponding i_{ds} will be less than that of (5.28), namely

$$i_{ds} < \frac{\lambda_{\mathrm{mf}} - \sqrt{\lambda_{\mathrm{mf}}^2 - 4(3ai_{qs}^2 + 2bi_{qs} + c - \mathrm{L_d})[(\mathrm{L_d} - c)i_{qs}^2 - bi_{qs}^3 - ai_{qs}^4]}}{2(3ai_{qs}^2 + 2bi_{qs} + c - \mathrm{L_d})} \tag{5.29}$$

And following from (5.13), one can obtain

$$\frac{d\ h(i_{qs})}{d\ i_{qs}} < 0 \tag{5.30}$$

whenever inequality (5.29) is satisfied. The inequality of (5.30) means that $h(i_{qs})$ is a monotonically decreasing function with respect to i_{qs}. In other words, the line current magnitude is increasing as i_{qs} is decreasing under the condition of (5.29). For a given torque T_e in (5.9), one can obtain

$$i_{ds} = \frac{(\frac{T_e}{0.75\mathrm{p}}) - \lambda_{\mathrm{mf}} i_{qs}}{(\mathrm{L_d} - ai_{qs}^2 - bi_{qs} - c)i_{qs}} \tag{5.31}$$

By taking the derivative of (5.31), one can get

$$\frac{di_{ds}}{di_{qs}} = \frac{i_{qs}(ai_{qs}^2 + bi_{qs} + c - \mathrm{L_d})[\lambda_{\mathrm{mf}} + (\mathrm{L_d} - 3ai_{qs}^2 - 2bi_{qs} - c)i_{ds}]}{[(\mathrm{L_d} - 3ai_{qs}^2 - 2bi_{qs} - c)i_{qs}]^2} \tag{5.32}$$

As the parameters of the tested IPMSM are concerned, one has

$$\lambda_{\mathrm{mf}} + (\mathrm{L_d} - 3ai_{qs}^2 - 2bi_{qs} - c)i_{ds} > 0 \tag{5.33}$$

over the full operational ranges of d- and q-axis currents. Thus, for $i_{qs} \in (0,\ \mathrm{I_{sm}})$, (5.32) is greater than zero. In other words, the constant torque curve on the $i_{ds}^* \sim i_{qs}^*$ plane is a monotonically increasing function of either i_{ds} or i_{qs}. In summary, when the proposed field weakening control is applied in either Region III or Region II for $T_e^* > T_{eb}$, the corresponding d- and q-axis current commands are chosen to be the ones corresponding to the intersection point of (5.20) and (5.23). And this intersection point is located to the left side of the curve of (5.15) as shown in Fig. 5.3. Thus, as has been shown that the d- and q-axis currents corresponding to the intersection point of (5.20) and (5.23) are smaller than that of the intersection point of (5.15) and (5.20) respectively. Since the line current magnitude is a monotonically decreasing function with respect to i_{qs}^* which has been shown in (5.30) so long as (5.29) is satisfied, also the operating point of the proposed field weakening control is chosen as the available largest i_{ds}^* and i_{qs}^* namely at the voltage limit curve, therefore the line current magnitude at the corresponding operating point for the proposed field weakening control is minimum within the feasible constant torque trajectory.

Finally, consider the transient control. For example, during the motor starting stage, while $\omega_r < \omega_{rM}$, the maximum torque (T_{eM}) can be applied to achieve the fastest response. However, when the motor speed is greater than ω_{rM}, the maximum torque T_{eM} cannot be achieved. Thus, for the proposed control strategy and for each ω_r, the corresponding

maximum torque, called T_{eMF}, can be obtained by first finding the corresponding d- and q-axis currents, namely I_{dsMF} and I_{qsMF} from (5.17) and (5.23) as:

$$I_{dsMF}^2 + I_{qsMF}^2 = \mathrm{I}_{\mathrm{sm}}^2 \tag{5.34}$$

$$g(I_{dsMF}, I_{qsMF}, \omega_r) = 0 \tag{5.35}$$

Then, the maximum torque and maximum virtual control becomes

$$T_{eMF}\Big|_{\omega_r} = 0.75\mathrm{p}\left[(\mathrm{L_d} I_{dsMF} + \lambda_{\mathrm{mf}}) I_{qsMF} - (aI_{qsMF}^3 + bI_{qsMF}^2 + cI_{qsMF}) I_{dsMF}\right] \tag{5.36}$$

$$u_{MF}\Big|_{\omega_r} = \frac{T_{eMF}\Big|_{\omega_r}}{\mathrm{K_{tM}}} \tag{5.37}$$

It should be mentioned that both I_{dsMF} and I_{qsMF} are functions of ω_r for $\omega_r \in (\omega_{rM}, \omega_{rE})$.

5.4 Implementation and Experimental Results

An implementation block diagram of the speed control is shown in Fig. 5.6 as an illustrative example. Except for the adaptive limiter block and the current commands calculator block, the other blocks are quite typical and will not be explained further. Actually, except for the adaptive limiter block and the current commands calculator block, the contents of the other blocks are the same as that in Fig. 4.5. First, consider the adaptive limiter block. From the proposed control strategy it is seen that for $\omega_r \le \omega_{rM}$, the maximum virtual control available is chosen to be

$$u_M = \frac{T_{eM}}{\mathrm{K_{tM}}} = \mathrm{I_{sm}},\ \omega_r \le \omega_{rM} \tag{5.38}$$

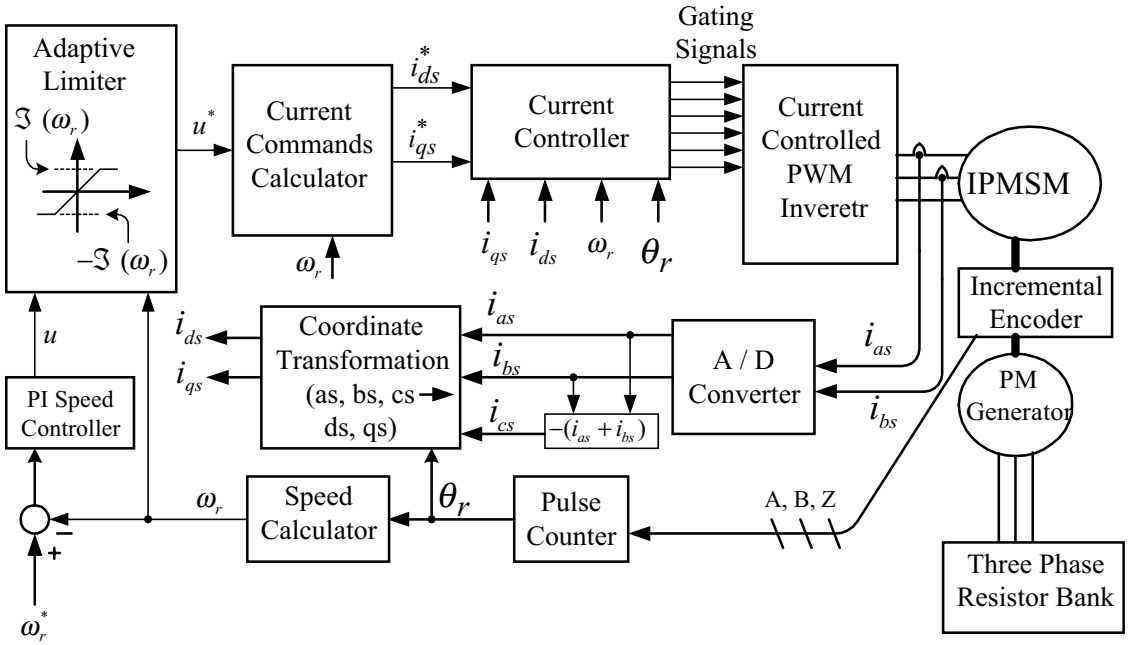

Fig. 5.6. Block diagram of the developed IPMSM drive system.

Also, for $\omega_r \in (\omega_{rM}, \omega_{rE})$, the maximum virtual control available is u_{MF} from (5.37). For easy implementation, one can define an adaptive limiter with the following adaptive upper bound

$$\Im(\omega_r) \triangleq \begin{cases} u_M = I_{sm}, & 0 \le \omega_r \le \omega_{rM} \\ u_{MF}\big|_{\omega_r}, & \omega_{rM} < \omega_r < \omega_{rE} \end{cases} \tag{5.39}$$

One can compare both adaptive upper bounds, namely $H(\omega_r)$ of (4.34) and $\Im(\omega_r)$ of (5.39). It is seen that they are two different functions because their corresponding torque equations use different q-axis flux linkage models. For reference, Fig. 5.7 shows a plot of the adaptive upper bound with $\omega_{rM} < \omega_r < \omega_{rE}$ for the tested IPMSM. Of course, when the output of the speed controller is not saturated, then the corresponding virtual control u^* is the same as the original u in this linear control region as shown in Fig. 5.6.

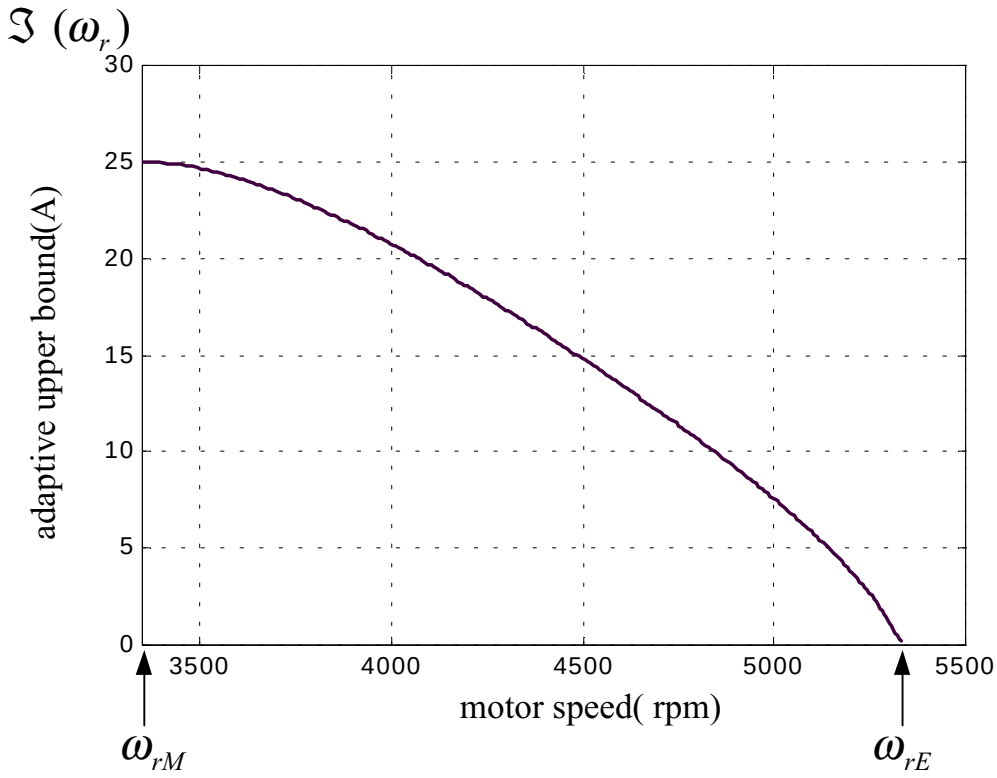

Fig. 5.7. Illustration of the adaptive upper bound to motor speed curve for the tested IPMSM.

Next, consider the current commands calculator. Fig. 5.8 shows the detailed flowchart of how to calculate the desired i_{ds}^* and i_{qs}^* for each virtual control u^* in different speed regions according to the proposed control strategy. One can see that the contents of the current commands calculator block in Fig. 5.6 is basically a modified version of that in Fig. 4.5. In other words, the flowchart of the current commands calculator block as shown in Fig. 5.8 is a modified version of that in Fig. 4.6. For simplifying the complicated calculation, the equations of i_{ds}^* and i_{qs}^* can be approximated from Fig. 5.2 using second order polynomials. These resulting two equations are listed as follows for the constant torque limit control:

$$i_{ds}^* = c_1(u^*)^2 + c_2 u^* + c_3 \tag{5.40}$$

$$i_{qs}^{*} = c_4 (u^{*})^2 + c_5 u^{*} + c_6 \tag{5.41}$$

where c_1 to c_6 are real constants. Similarly, for each $\omega_r \in (\omega_{rM}, \omega_{rE})$ in the field weakening control, the corresponding i_{ds}^{*} and i_{qs}^{*} are the solutions of (5.20) and (5.23). They can also be approximated by the following expressions:

$$i_{ds}^{*} = w_1 (u^{*})^2 + w_2 u^{*} + w_3 \tag{5.42}$$

$$i_{qs}^{*} = w_4 (u^{*})^2 + w_5 u^{*} + w_6 \tag{5.43}$$

Since the values of w_1 to w_6 in (5.42) and (5.43) now varies with ω_r for each $\omega_r \in (\omega_{rM}, \omega_{rE})$, the second order polynomial approximation can also be used to fit the w_k coefficients for k=1, 2, …, 6 as follows:

$$w_k = c_{k1} \omega_r^2 + c_{k2} \omega_r + c_{k3} \tag{5.44}$$

with c_{kj}, $k = 1, 2, ..., 6$, $j = 1, 2, 3$ being real constants. From actual experiments, it is found that, with the above approximations, the errors between the actual current commands and the approximated current commands for both d- and q-axis are less than 1.4% (or 0.35 A), but the calculation time is greatly reduced.

In order to verify the feasibility of the proposed control strategy, a prototype is constructed according to the block diagram of Fig. 5.6 by using a fixed-point DSP TMS320F240. The sampling time periods for the current controller and the speed controller are chosen to be 0.1 msec and 1 msec respectively. The tested IPMSM, a prototype designed

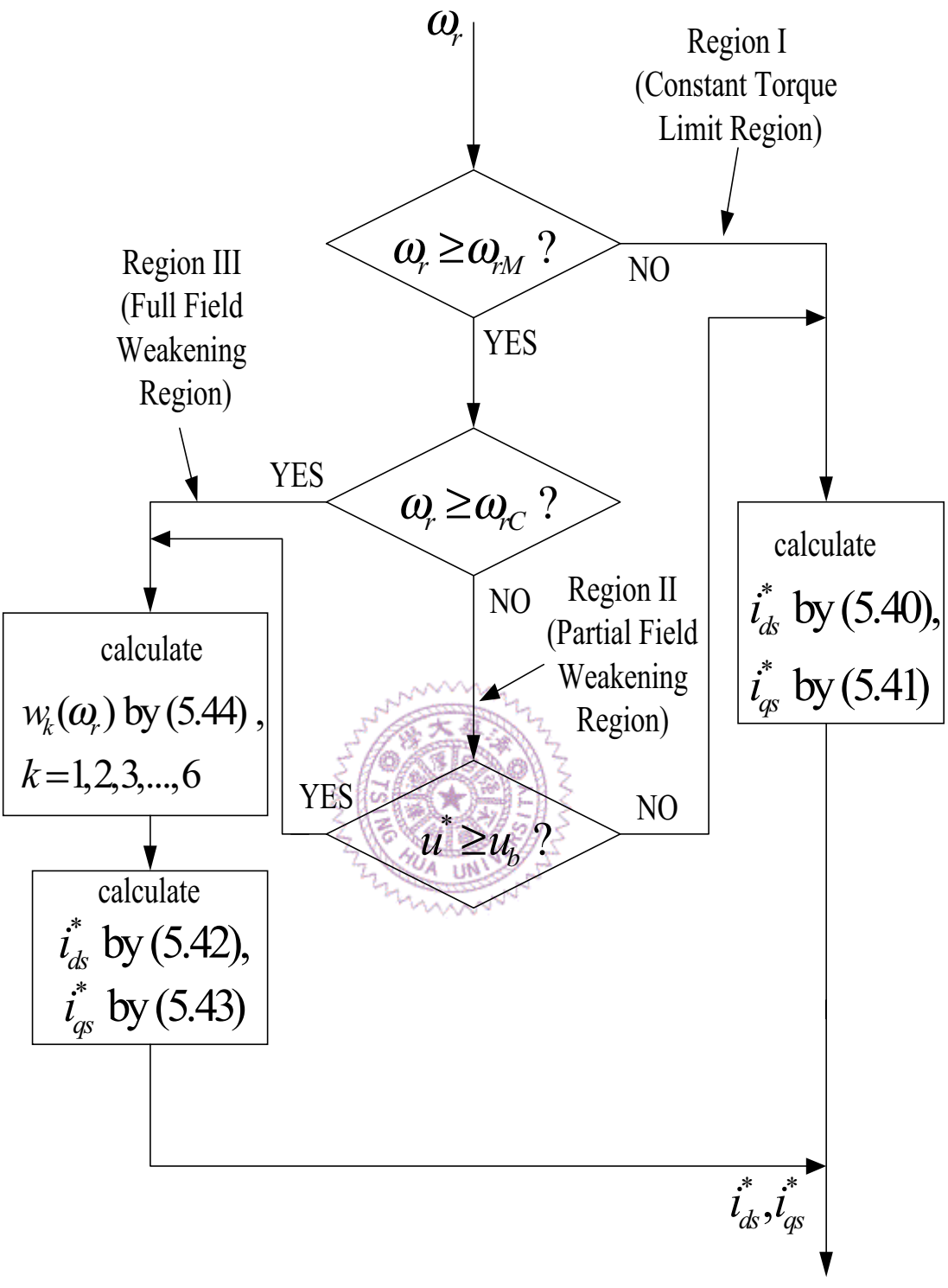

Fig. 5.8. The flowchart of the current commands calculator in Fig. 5.6.

in [67], has the same parameters as given in Table 5.1. The corresponding ω_{rM} and ω_{rC} are found to be 3340 rpm and 3790 rpm from (5.19) and (3.3) respectively. Similarly, the I_{dsM} and I_{qsM} are –3.2(A) and 24.8(A) from solving the system of equations of (5.15) and (5.17). For reference, the DSP program code for the speed controlled IPMSM drive is listed in APPENDIX A.

In the dissertation, all the control functions of the drive system are implemented fullly digital by using a DSP TMS320F240, the hardware circuits are greatly simplified. The current controlled PWM inverter in the system block diagram of Fig. 5.6 is a three phase voltage source inverter. For reference, the corresponding electric circuit is shown in Fig. 5.9 where the DC link voltage V_{DC} is supplied by a DC power supply and the power semiconductor switches are six insulated gate bipolar transistors (IGBTs). The corresponding six gate driver circuits in Fig. 5.10 are used to drive the IGBTs of the inverter. Six input signals of the gate drivers are the output gating signals of the DSP as shown in Fig. 5.6. To obtain the line current signals, two commercial Hall effect current sensors named

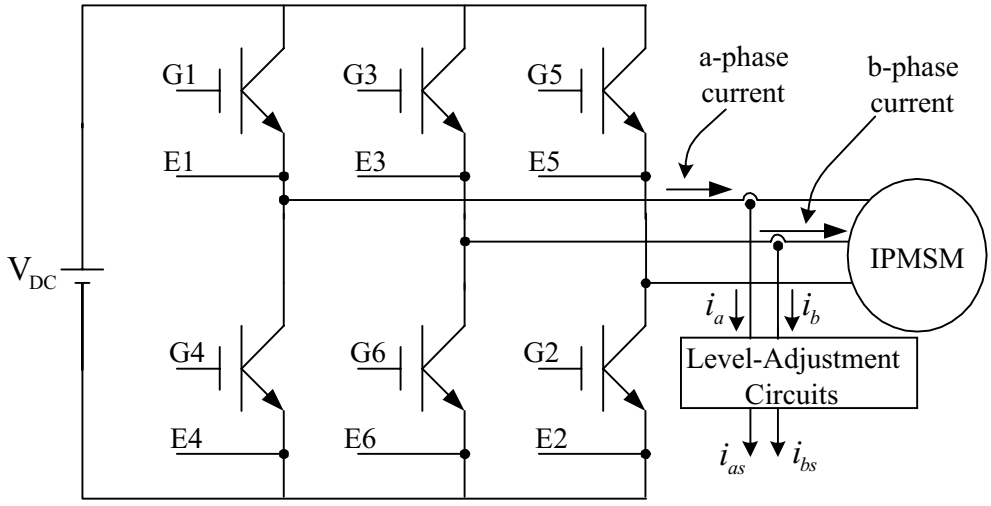

Fig. 5.9. Circuit configuration of the three phase voltage source inverter.

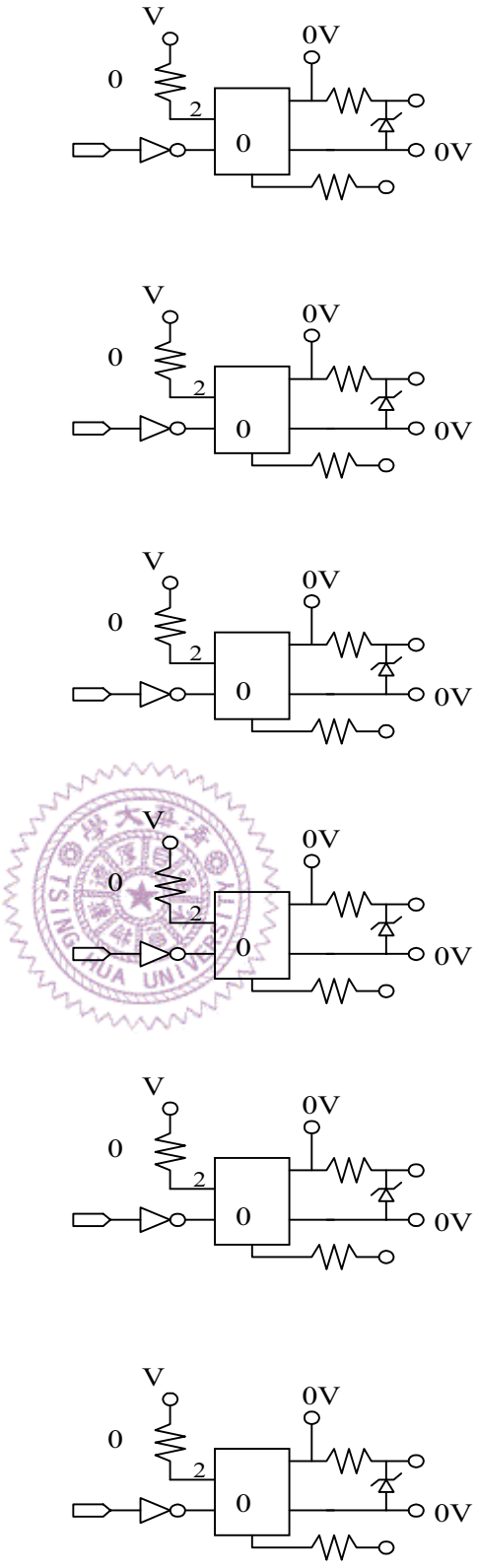

Fig. 5.10. Six gate driver circuits of the inverter.

LEM HAS50-S, are used to induce the phase a and b currents into the signals i_a and i_b respectively. As can be seen in Fig. 5.9, the signals i_a and i_b are connected to the level-adjustment circuits to generate the signals of i_{as} and i_{bs}. Actually, the signals of i_{as} and i_{bs} (i.e. the outputs of the level-adjustment circuits in Fig. 5.9) are to accommodate the input voltage range of the A/D converter in the DSP chip. The corresponding level-adjustment circuits are shown in Fig. 5.11. Finally, a picture of a prototype of the IPMSM drive system constructed in the advisor's laboratory is shown in Fig. 5.12 and a rotor cross section view of the tested IPMSM is also shown in Fig. 5.13.

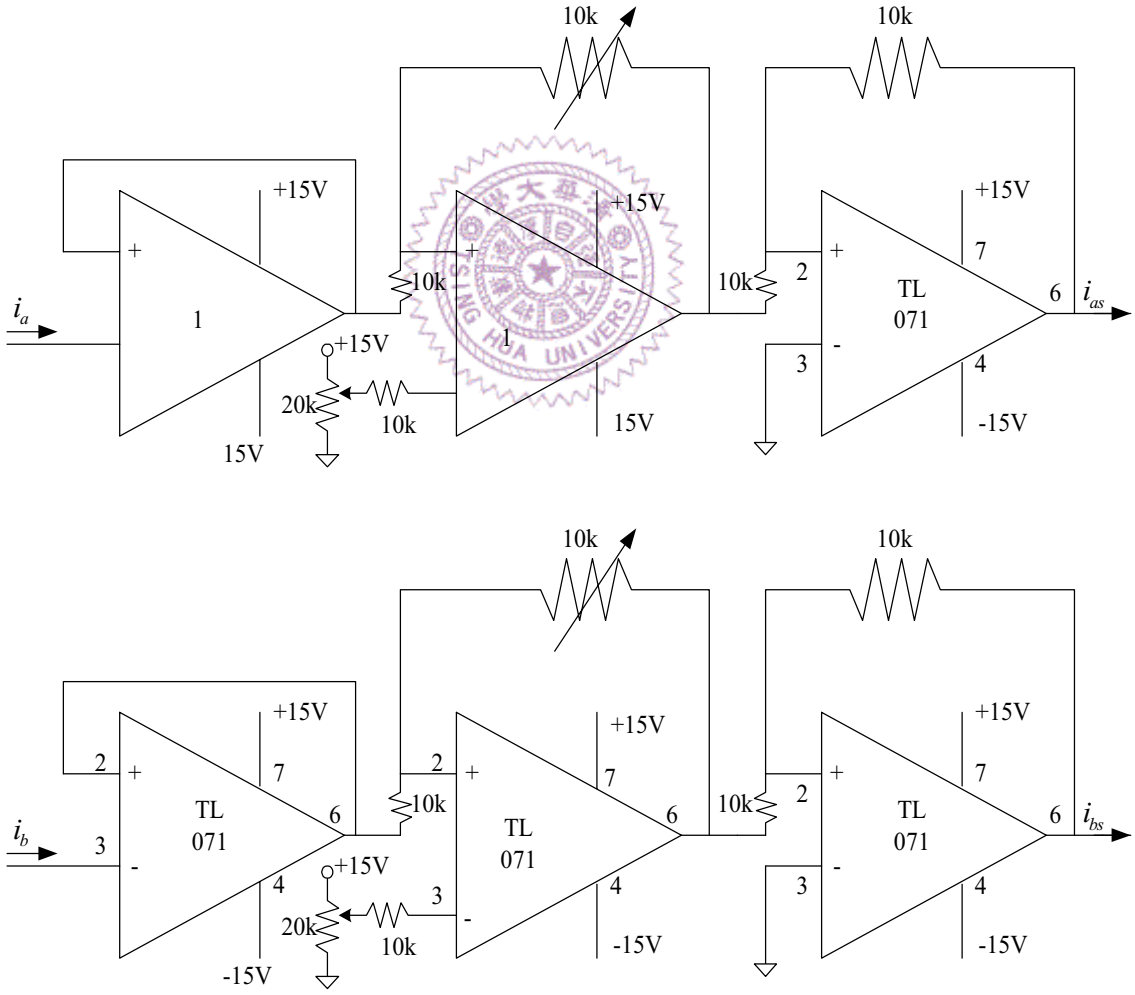

Fig. 5.11. The level–adjustment circuits of i_{as} and i_{bs}.

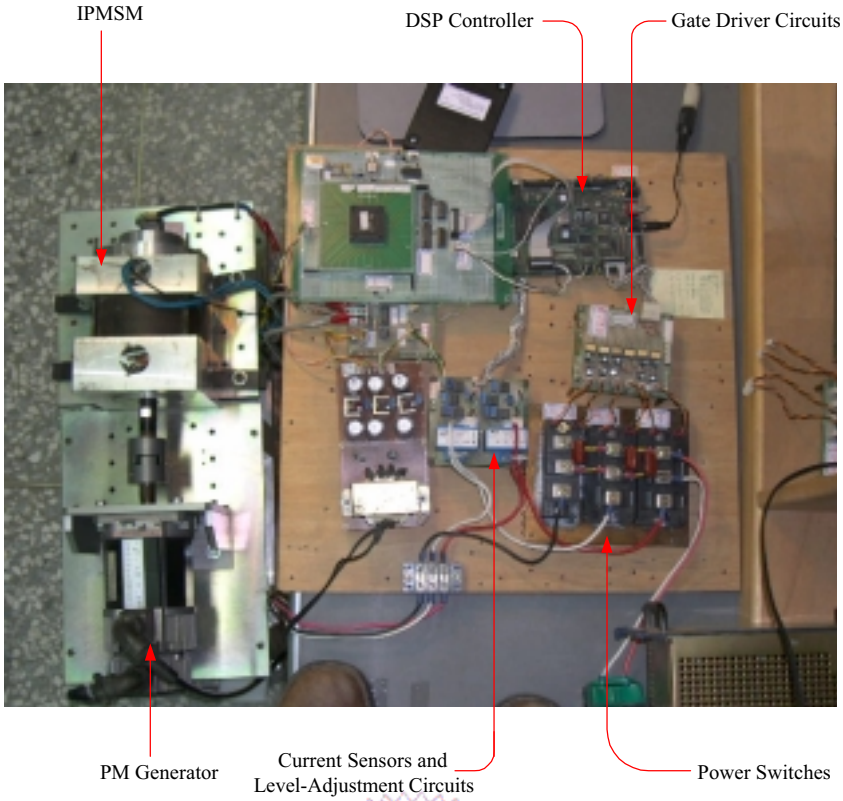

Fig. 5.12. Picture of a prototype of the IPMSM drive system.

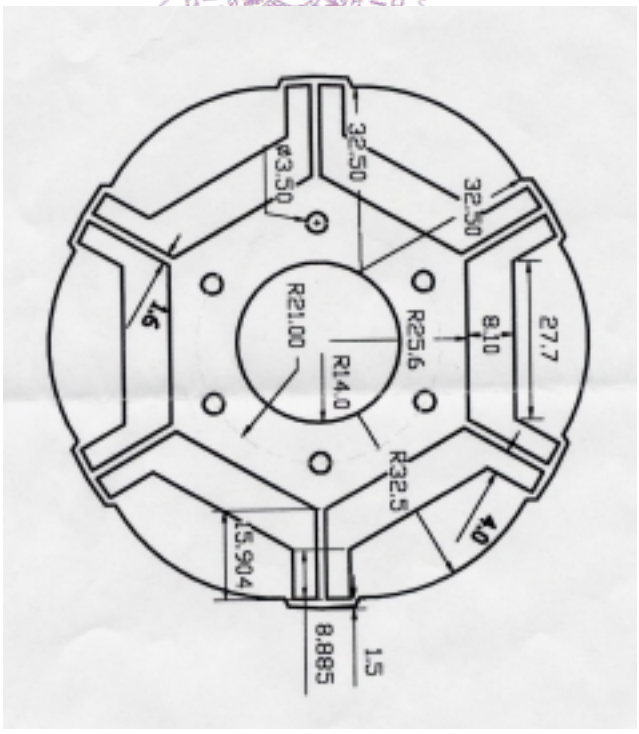

Fig. 5.13. A rotor cross section view of the tested IPMSM.

Some experimental results are presented to compare the performances of the proposed LMTPA control with and without considering saturation effect in the constant torque limit region, the partial field weakening region, and the full field weakening region respectively. Firstly, consider the case of applying a step command of ω_r^*=3000 rpm to the tested IPMSM drive starting from rest at t=0 sec. The corresponding steady state load torque at 3000 rpm is approximately 3.2 Nm. This test is to demonstrate the characteristics of the transient response as well as the steady state response in the constant torque limit region as the saturation effect is not considered in the control algorithms of the drive. Fig. 5.14 shows the corresponding waveforms of the d- and q-axis current responses and speed response. The corresponding I_{dsM} and I_{qsM} are approximately –6.6(A) and 24.1(A) respectively as calculated in Chapter 4. From Fig. 5.14 one can see that the acceleration time period is approximately 820 msec. Fig. 5.15 also records the waveforms of the phase-a current and the speed response corresponding to Fig. 5.14 except that the corresponding waveform recording time is longer than that of Fig. 5.14. The steady state waveform of phase-a current corresponding to Fig. 5.15 is also shown in Fig. 5.16. One can see that the root mean square value of phase-a current is 12.74(A).

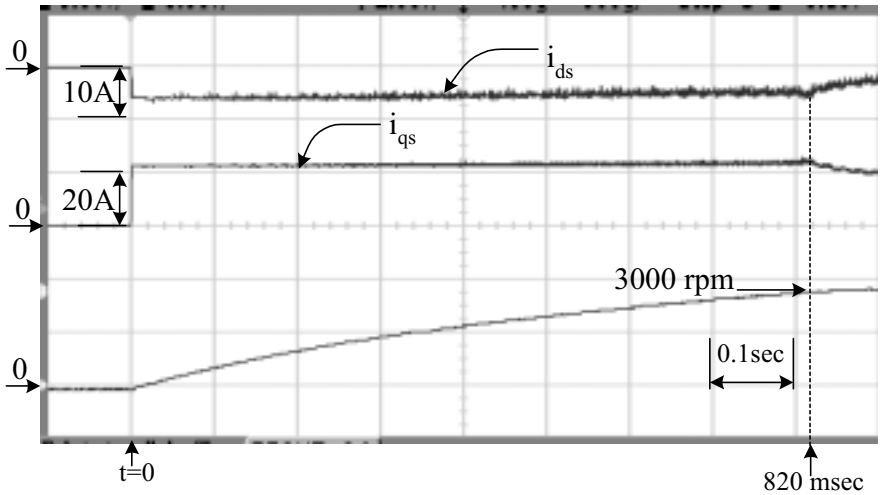

Fig. 5.14. Experimental results of i_{ds}, i_{qs}, and motor speed responses within the constant torque limit region without considering magnetic saturation.

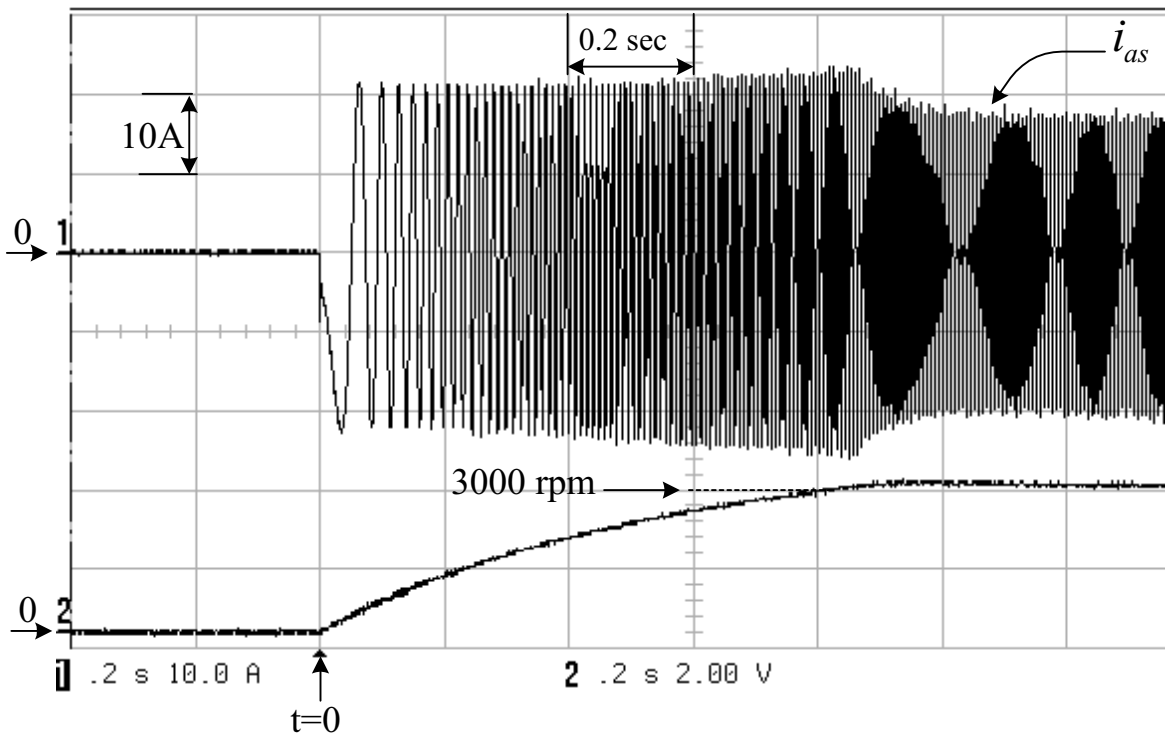

Fig. 5.15. The waveforms of the phase-a current response and the speed response corresponding to Fig. 5.14.

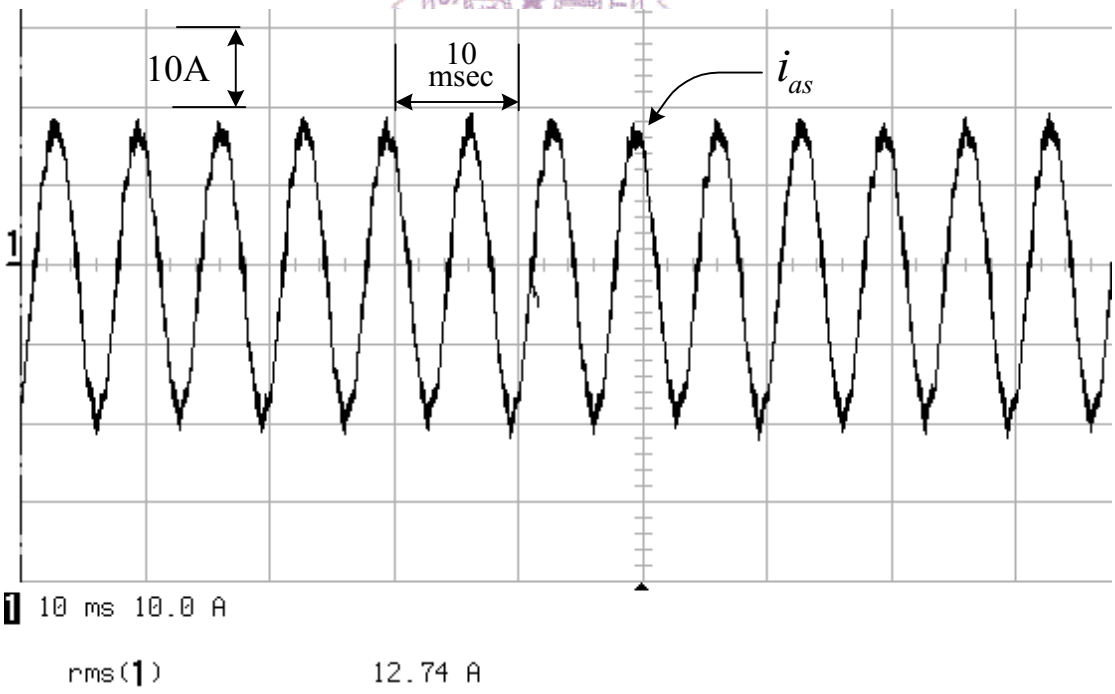

Fig. 5.16. The steady state waveform of phase-a current corresponding to Fig. 5.15.

Next, consider the same test except that the saturation effect of the tested IPMSM is considered in the control algorithms of the drive system, all other test conditions and the controller parameters are kept the same as the previous one. Fig. 5.17 shows the corresponding waveforms of the d- and q-axis current responses and speed response. The corresponding I_{dsM} and I_{qsM} are approximately –3.22(A) and 24.8(A) respectively as calculated from solving the system of equations of (5.15) and (5.17). Fig. 5.17 shows that the acceleration time period is approximately 760 msec which is shorter than that of Fig. 5.14 by 7.3%. Fig. 5.18 also records the waveforms of the phase-a current and the speed response corresponding to Fig. 5.17. The steady state waveform of phase-a current is also shown in Fig. 5.19. One can see that the root mean square value of phase-a current is 12.4 A approximately which is smaller than that of Fig. 5.16 by 2.7%.

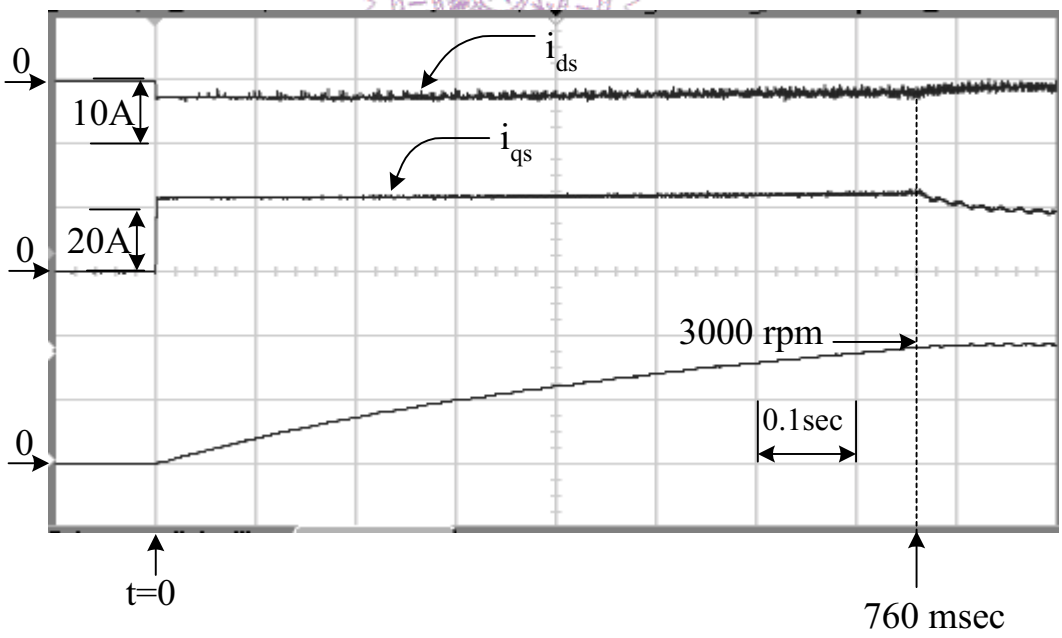

Fig. 5.17. Experimental results of i_{ds}, i_{qs}, and motor speed responses within the constant torque limit region with consideration of magnetic saturation.

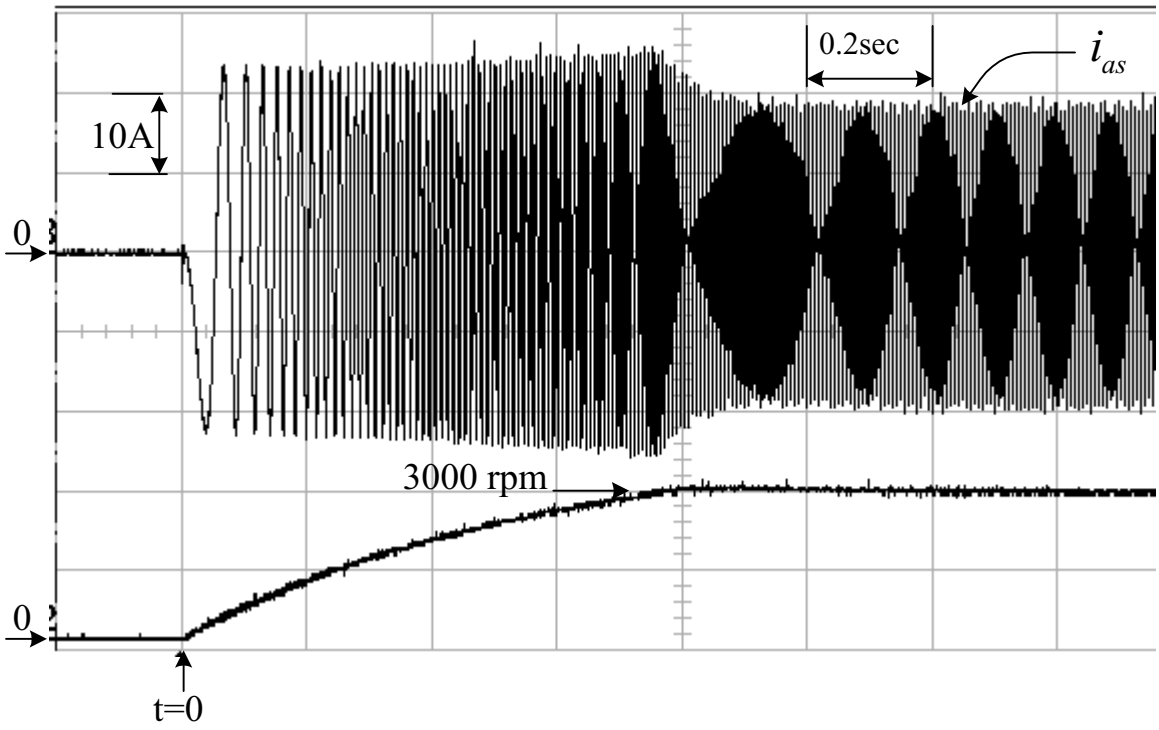

Fig. 5.18. The waveforms of the phase-a current response and the speed response corresponding to Fig. 5.17.

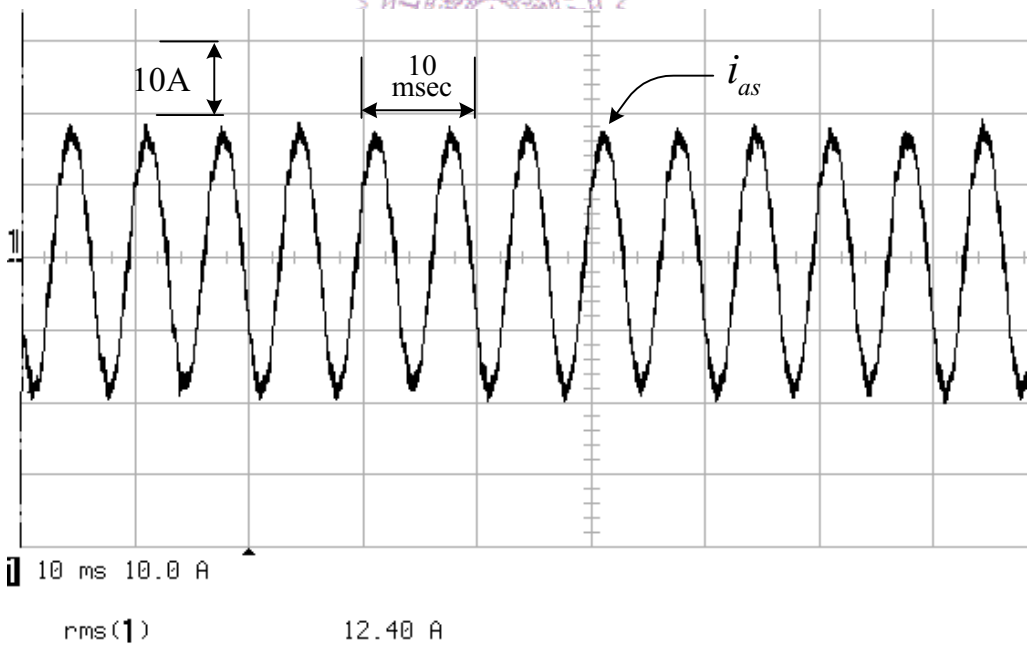

Fig. 5.19. The steady state waveform of phase-a current corresponding to Fig. 5.18.

Secondly, to demonstrate the characteristics of the transient responses in the partial field weakening region, one considers the case of applying a step command of ω_r^*=3700 rpm to the tested IPMSM drive starting from rest at t=0 sec. Figs. 5.19 and 5.20 show the waveforms of the d- and q-axis current responses and speed responses without and with considering magnetic saturation effect respectively. One can observe that the acceleration times of the IPMSM with and without considering magnetic saturation are approximately 590 msec and 570 msec respectively which means that the maximum torque with considering magnetic saturation is larger than that without considering magnetic saturation. The accelerating time period with considering magnetic saturation effect is shorter than that without considering saturation effect by 3.4%. Next, considering the steady state operation condition in the partial field weakening region. Figs. 5.21 to 5.24 show the response waveforms of the phase-a current and the speed without and with considering magnetic saturation respectively while all the test conditions are kept the same as previous one except that a heavier load is applied. Figs. 5.22 and 5.24 are the corresponding steady state waveforms of phase-a current of Figs. 5.21 and 5.23 respectively. From Fig. 5.23 and Fig. 5.25, one also can observe that the root mean square value of the phase-a current with considering magnetic saturation is 8.92 A which is smaller than that without considering magnetic saturation by 4.2%. It also implies that the copper loss can be reduced in the partial field weakening region by considering magnetic saturation.

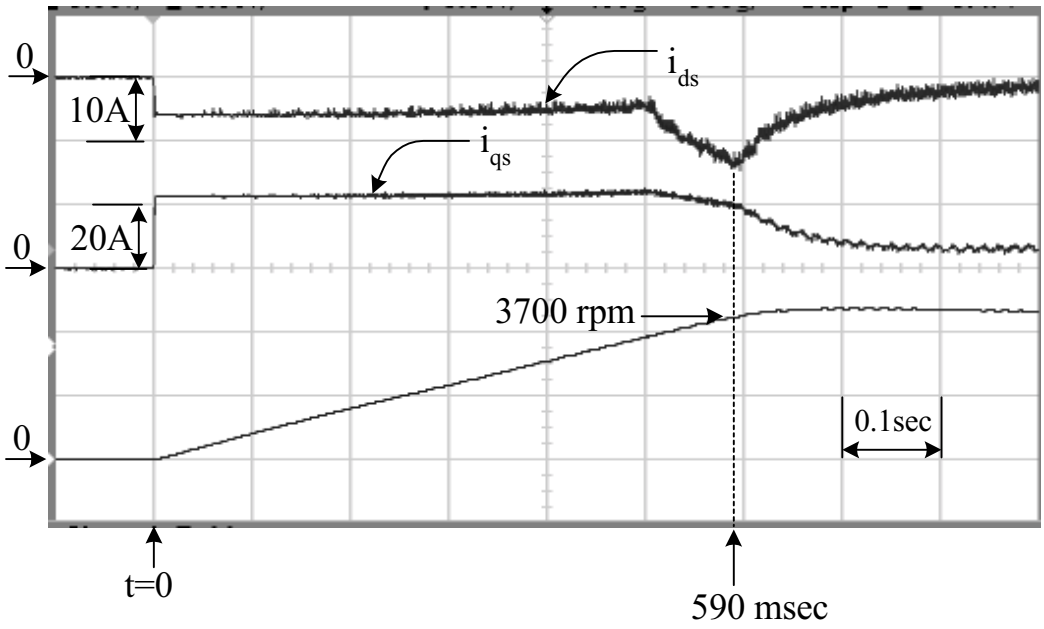

Fig. 5.20. Experimental results of i_{ds}, i_{qs}, and motor speed responses while accelerating toward the partial field weakening region without considering magnetic saturation.

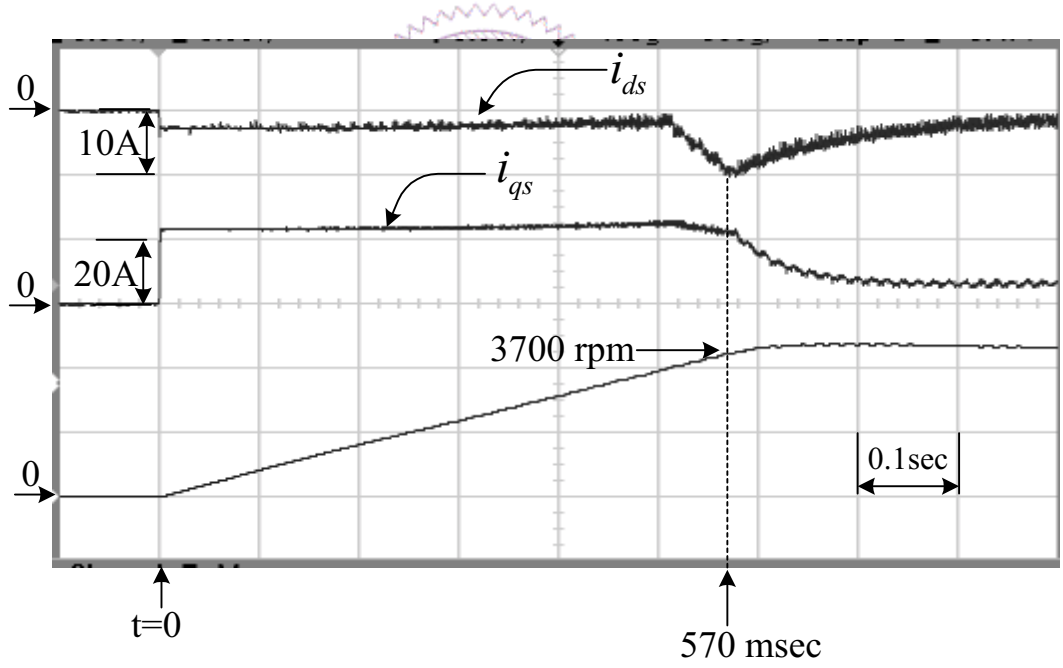

Fig. 5.21. Experimental results of i_{ds}, i_{qs}, and motor speed responses while accelerating toward the partial field weakening region with considering magnetic saturation.

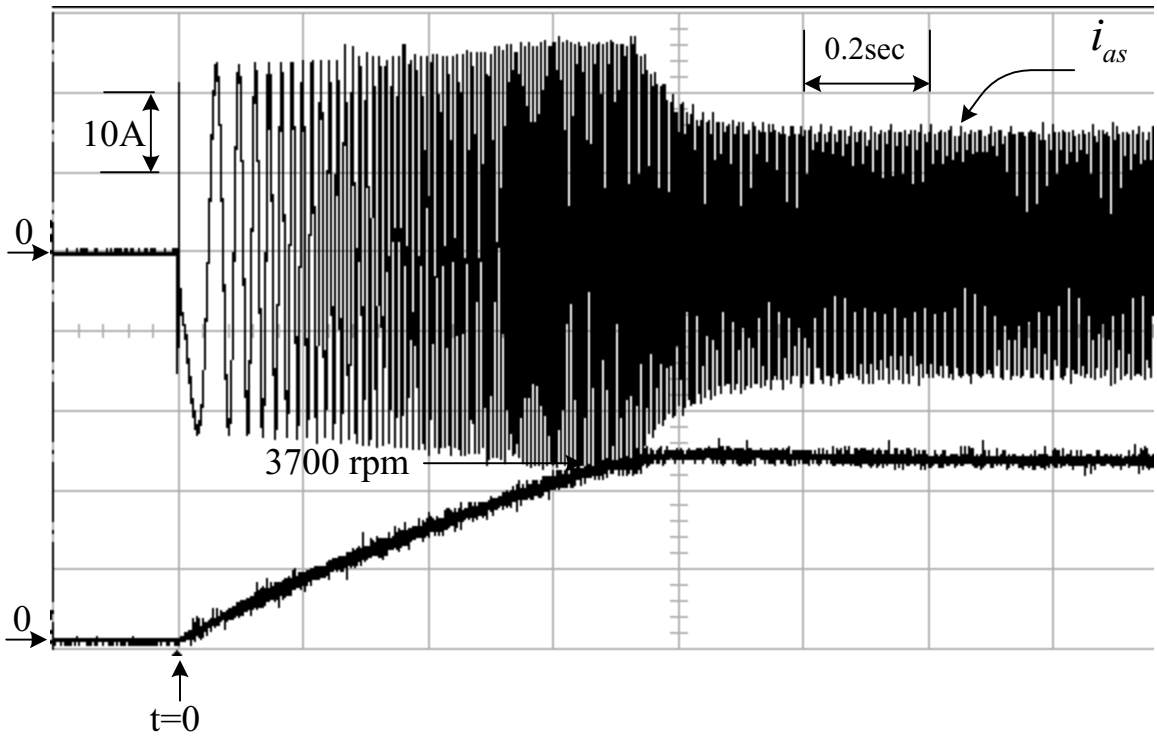

Fig. 5.22. The waveforms of the phase-a current response and the speed response while accelerating toward the partial field weakening region with heavier load and without considering magnetic saturation.

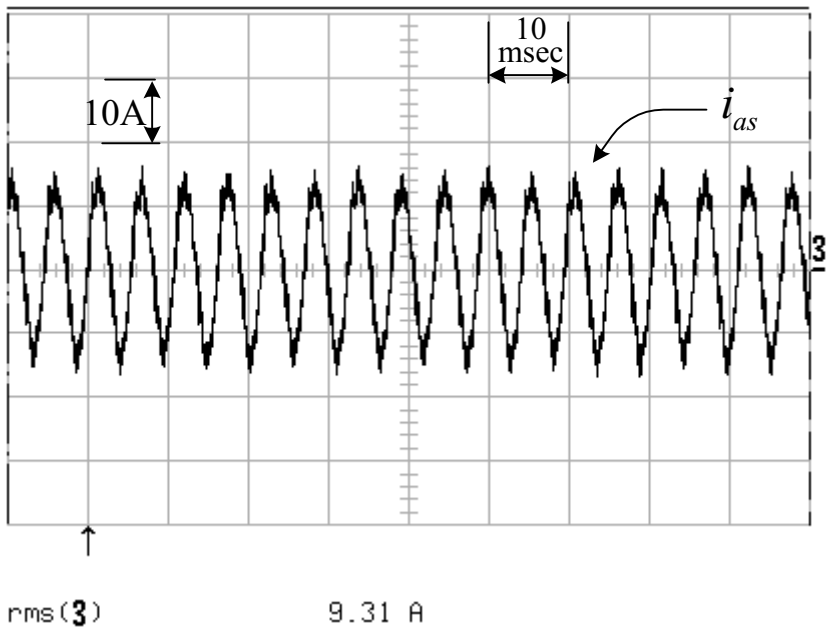

Fig. 5.23. The steady state waveform of phase-a current corresponding to Fig. 5.22.

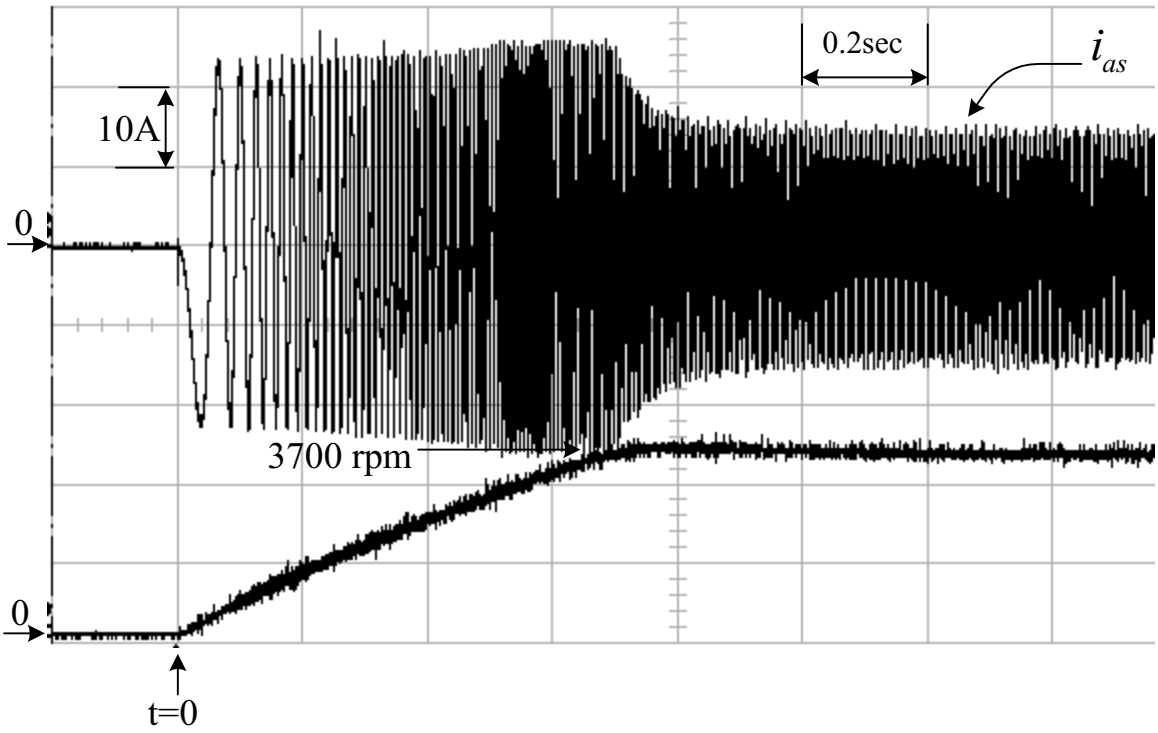

Fig. 5.24. The waveforms of the phase-a current response and the speed response while accelerating toward the partial field weakening region with heavier load and considering magnetic saturation.

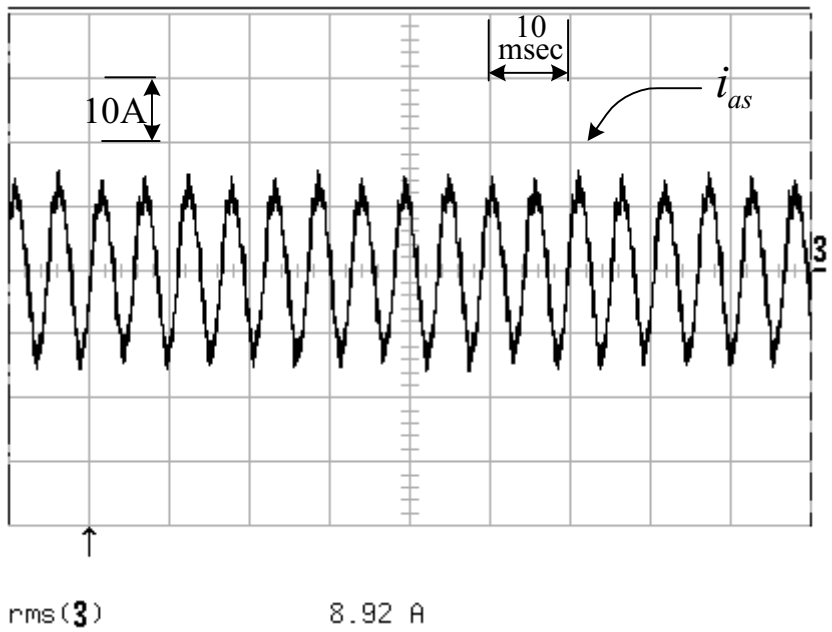

Fig. 5.25. The steady state waveform of phase-a current corresponding to Fig. 5.24.

Finally, to demonstrate the characteristics of the transient responses as well as the steady state responses in the full field weakening region, one considers the case of applying a step command of f ω_r^*=4300 rpm to the tested IPMSM drive starting from rest at t=0 sec. Figs. 5.25 and 5.26 show the waveforms of the d- and q-axis current responses and the speed response without and with considering magnetic saturation respectively. From these two waveforms, one can observe that the acceleration times of the tested IPMSM are approximately 780 msec and 740 msec respectively. The accelerating time period with considering magnetic saturation effect is shorter than that without considering magnetic saturation effect by 5.1%. It can be said that the maximum torque with considering magnetic saturation is also larger than that without considering magnetic saturation in the full field weakening region. Figs. 5.27 and 5.29 show the response waveforms of the phase-a current and the speed without and with considering magnetic saturation respectively corresponding to the previous full field weakening test condition. And Figs. 5.28 and 5.30 are the corresponding steady state response waveforms of the phase-a current of Figs. 5.27 and 5.29 respectively. From Figs. 5.28 and 5.30, one can see that the root mean square value of the steady state phase-a current with considering magnetic saturation is 10.59 A which is smaller than that without considering magnetic saturation by 1.12%. It also can be concluded that the copper loss can be reduced in the full field weakening region with considering magnetic saturation.

From the above experimental results, one can see that within all the three speed ranges, the truly maximum torque of the tested IPMSM drive can be achieved by considering the magnetic saturation and the corresponding transient performance can be enhanced by at least 3.4%. Again within all the three speed ranges, the steady state line current magnitude can be

reduced for the tested IPMSM drive by considering the magnetic saturation and the corresponding copper loss can be reduced by about 2.7% on average. These experimental results clearly demonstrate the improvement of the dynamic as well as the steady state performances of the tested IPMSM drive if the magnetic saturation effect is properly corrected..

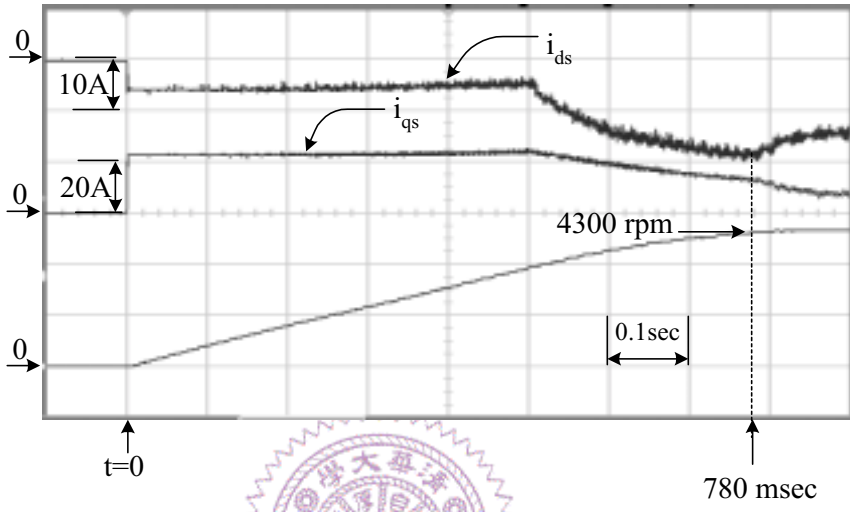

Fig. 5.26. Experimental results of i_{ds}, i_{qs}, and motor speed responses while accelerating toward the full field weakening region without considering magnetic saturation.

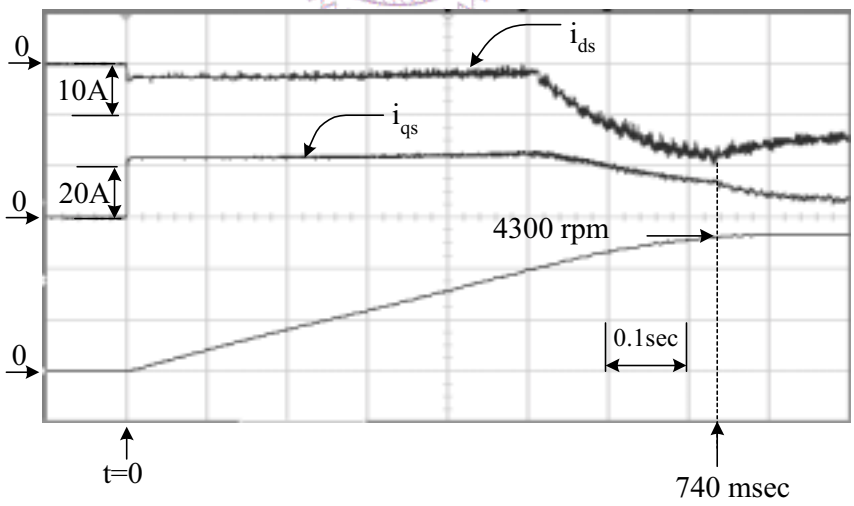

Fig. 5.27. Experimental results of i_{ds}, i_{qs}, and motor speed responses while accelerating toward the full field weakening region with considering magnetic saturation.

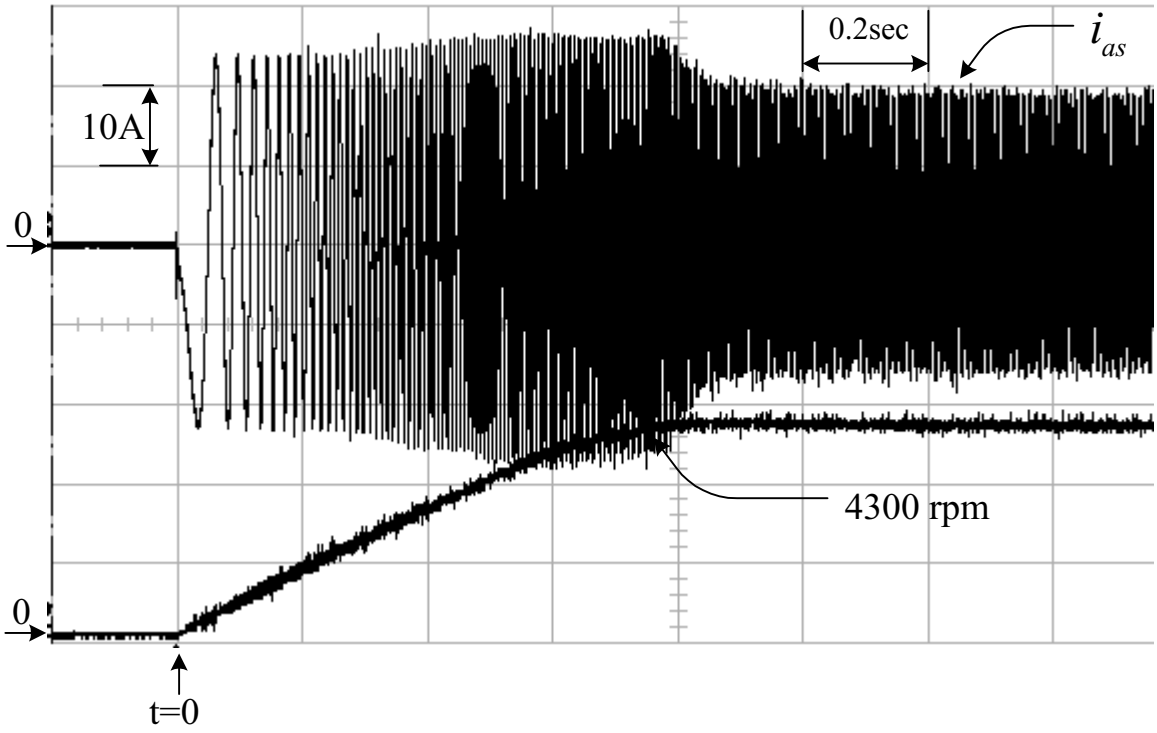

Fig. 5.28. The waveforms of the phase-a current response and the speed response corresponding to Fig. 5.26.

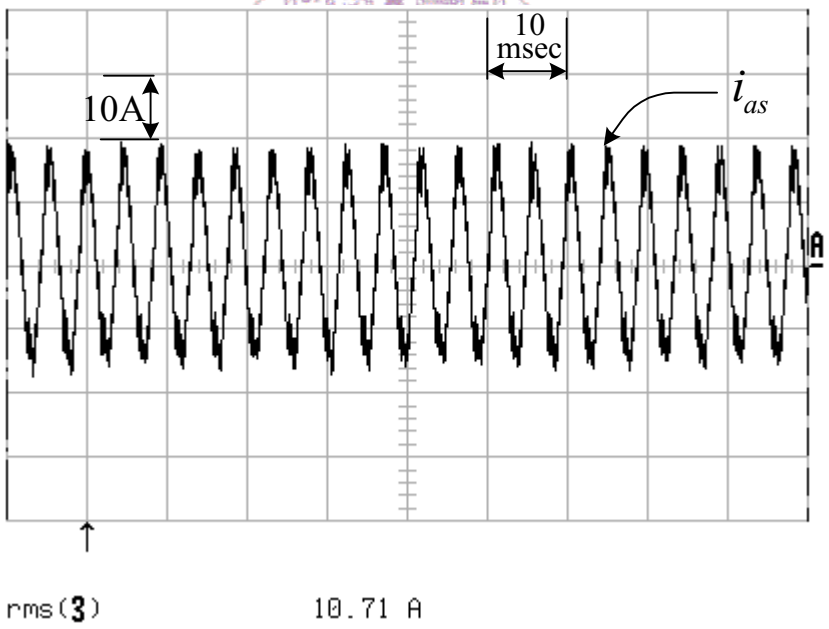

Fig. 5.29. The steady state waveform of the phase-a current corresponding to Fig. 5.28.

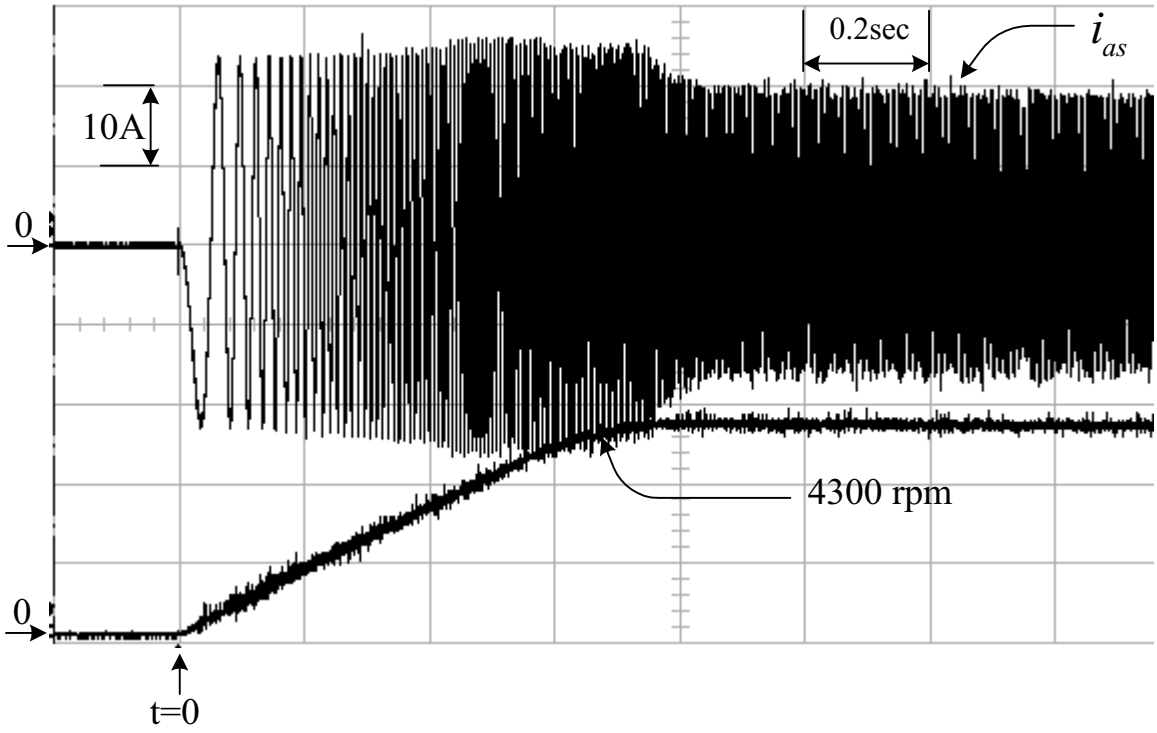

Fig. 5.30. The waveforms of the phase-a current response and the speed response corresponding to Fig. 5.27.

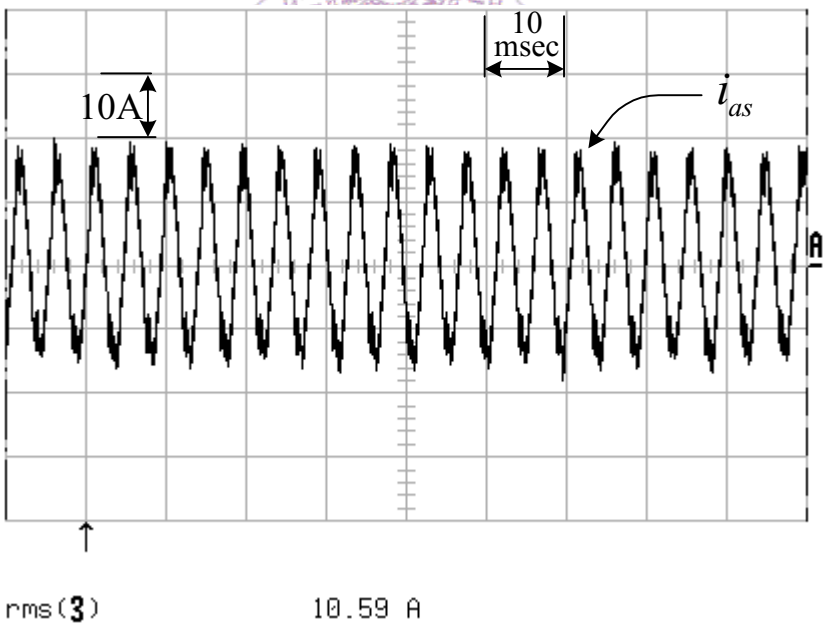

Fig. 5.31. The steady state waveform of the phase-a current corresponding to Fig. 5.30.